Capturing and Attributing the Rainfall Regime Intensification in the West African Sahel with CMIP6 Models

G. CHAGNAUD,[a] G. PANTHOU,[a] T. VISCHEL,[a] AND T. LEBEL[a]

[a] *Université Grenoble Alpes, CNRS, IRD, Grenoble INP, IGE, Grenoble, France*

(Manuscript received 1 June 2022, in final form 15 November 2022)

ABSTRACT: Rainfall in the Sahel is extremely variable on daily to multidecadal time scales, challenging climate models to realistically simulate its past and future evolution and questioning their relevance for defining suitable climate change adaptation strategies. Improving confidence in climate models may be achieved by (i) evaluating their capacity for reproducing observed climatic evolution and (ii) attributing these evolutions. Moreover, there is a need to consider relevant climatic indicators, from an end-user point of view. Fully coupled (CMIP6-AOGCM) models with idealized detection and attribution forcings (DAMIP) as well as atmosphere-only simulations (AMIP) are used to investigate the respective roles of external forcing factors and internal climate variability in the observed intensification of the Sahelian rainfall regime. We show that CMIP6 models contain signs of the intensification of the rainfall regime as detected over the past 35 years from a regional daily observations network. Both the increase in intensity and occurrence of wet days, as well as that of extreme daily rainfall, are remarkably well reproduced by historical simulations incorporating anthropogenic forcing factors, with anthropogenic aerosols contributing the largest share of this trend. Though more strongly affected by model structure uncertainty, the greenhouse gas forcing also displays noticeably robust features. Models are shown to fail at simulating the observed dry extreme evolution. These findings give incentive for further investigating the underlying physical mechanisms that drive the Sahelian rainfall regime evolution at regional to subregional scales. Furthermore, future hydroclimatic trajectories in the Sahel should be explored, though particular caution is required as to which rainfall indicator to consider.

SIGNIFICANCE STATEMENT: The rainfall regime at a particular location is crucial to human and ecosystem livelihoods. Changes in rainfall regime characteristics on multidecadal time scales result from both the effects of external forcing factors on the climate and of its internal variability, with this latter aspect becoming more prominent on small spatial scales. In this study, several state-of-the-art climate simulations are used to document the rainfall regime evolution of the past 65 years in the Sahel, in terms of amplitude, timing, and causes. It is shown that large-scale anthropogenic factors have a substantial imprint, modulated to some extent by internal variability. These findings demonstrate that coarse-resolution climate models are a well-suited tool to investigate the recent intensification of rainfall in the Sahel, and may provide valuable information for climate change adaptation planning.

KEYWORDS: Monsoons; Rainfall; Climate models; Decadal variability; Trends; Anthropogenic effects/forcing

1. Introduction

a. *Detecting and attributing rainfall regime intensification at a regional scale*

As highlighted by the various IPCC-AR6 reports (Masson-Delmotte et al. 2021; Pörtner et al. 2022), the regional dimension of climate change is becoming a central concern for both the scientific community and stakeholders worldwide, for a number of concurring reasons. For scientists, hierarchizing and understanding the interplays between the various processes that control the impact of global warming on regional climates remain a puzzling challenge; this has essential consequences for the capacity of climate models to properly reproduce the ongoing evolution of local to regional[1] climate features, especially when it comes to the water cycle in general and precipitation in particular. For stakeholders, the central issue is that climate change itself as well as its impacts on every aspect of life are felt locally; they thus need an assessment of the confidence they can put in rainfall scenarios at the appropriate scales. At the intersection of the challenges faced by these two communities of actors lies the detection–attribution issue. A first step for gaining confidence in climate models is to evaluate whether they capture the multiscale rainfall evolution in regions where such evolution has been detected in observations. A second step is to identify and rank the changes of forcing factors accounting for the detected evolution; such attribution studies are necessary for anticipating the impact of future forcing factor changes (Hegerl et al. 2019). Linking ongoing detected trends to expected future changes through attribution studies is, in turn, essential for the elaboration of relevant adaptation policies in territories where populations have

Supplemental information related to this paper is available at the Journals Online website: https://doi.org/10.1175/JCLI-D-22-0412.s1.

Corresponding author: Guillaume Chagnaud, guillaume.chagnaud@univ-grenoble-alpes.fr

[1] In this study, unless otherwise stated, the term "regional" refers to spatial scales ranging from hundreds to thousands of kilometers [see Doblas-Reyes et al. (2021), their section 10.1.2.].

DOI: 10.1175/JCLI-D-22-0412.1

already to adapt to new climate conditions while questioning what is coming next.

Detecting rainfall regime evolution in climate models at regional scale and attributing them to a modification of the external forcing combination is challenging in two main respects: one is linked to the intermittent nature of rainfall while the other is linked to the way rainfall-producing processes are represented in models.

The highly variable and multiscale nature of rainfall implies that climate modifications may have different consequences at different scales. For instance, at the global scale, the expected change in mean annual precipitation due to CO_2-driven warming is estimated to $\approx$2.5% K^{-1} (Fläschner et al. 2016; Allan et al. 2020; Pendergrass 2020). On the other hand, it may reach much larger values at local/convective scale where local phase equilibrium dominates, typically following the Clausius–Clapeyron law at a rate of $\approx$6.5% K^{-1} (Trenberth 1999; Allen and Ingram 2002; Held and Soden 2006; Pall et al. 2007), or even bigger given the ability of large convective systems for pumping atmospheric moisture far away from the core of the system (Trenberth et al. 2003). In-between these two scale extrema, a range of different behaviors may exist, most notably when global warming modifies the regional climate dynamics, possibly involving a decrease of the mean annual precipitation. It is thus expected that, in some regions, the mean annual precipitation may increase only slightly, or even decrease, while the extreme rainfall values increase, especially in tropical regions where rainfall occurrences and intensities are jointly driven by monsoon dynamics at regional scale and convection at local scale.

The representation of rainfall-producing processes in climate models is another source of difficulty when it comes to detecting meaningful changes in their rainfall outputs in conjunction with changing forcing factors. On the one hand, global-scale energetic constraints—driving the response of global-mean annual precipitation to any modification of the atmospheric composition (mainly GHG and aerosols)—are well resolved by models (Allen and Ingram 2002; Stephens and Ellis 2008; Pendergrass and Hartmann 2014). On the other hand, the subscale processes are ill-represented in most climate models for both resolution and parameterization reasons. This is especially problematic in tropical regions where the interactions between thermodynamical processes (e.g., phase equilibrium laws, convection) and dynamical processes (e.g., regional monsoon dynamics) play a key role in shaping rainfall regimes. Capturing regional rainfall regime evolution with climate models may thus largely depend on their capacity to correctly simulate thermodynamical aspects as well as atmospheric and oceanic circulation patterns, and their coupling.

The Sahel is typically one of these tropical regions where thermodynamical and dynamical factors combine in a puzzling way, and where any rainfall regime modification affects directly and importantly the living conditions of the population. It is thus a well-positioned region for testing the ability of an array of climate models to detect a well-established ongoing rainfall regime change and for looking at their attribution capacity.

b. *Region of study*

Over the twentieth century, the Sahelian annual rainfall variability has displayed a strong decadal mode (e.g., Nicholson et al. 2018). From the 1950s onward, this decadal variability was strongly amplified, with a shift from anomalously wet decades (1950–60s) to the 1970–80s dry decades, resulting in a regional long-lasting drought (Hulme 2001; Dai et al. 2004). An increase in annual rainfall was then observed, starting at the end of the 1980s (Nicholson 2005; Lebel and Ali 2009; Sanogo et al. 2015). Such an evolution results from the complex interplay between internal climate variability (ICV) and external forcing factors. On the one hand, the wet–dry swing of the 1950–90 period has been suggested to originate mainly in the switching from a positive to a negative phase of the Atlantic multidecadal oscillation (AMO; Zhang and Delworth 2006; Mohino et al. 2011), an internally generated pattern of sea surface temperature (SST, Ting et al. 2009; Friedman et al. 2020) whose link with Sahel rainfall is robustly captured by climate models (Ting et al. 2011; Lyu and Yu 2017). At the same time, anthropogenic aerosols emissions have been shown to produce a longer-term overall drying of the Sahel (Rotstayn and Lohmann 2002; Biasutti and Giannini 2006; Ackerley et al. 2011) through their control on Atlantic SSTs (Hoerling et al. 2006; Booth et al. 2012). On the other hand, the partial recovery of the last decades seems to be a combination of an increase in greenhouse gases (GHG) concentrations (Dong and Sutton 2015; Park et al. 2016) and the decline of anthropogenic aerosols concentrations (Giannini and Kaplan 2019; Marvel et al. 2020), with the reversal of the AMO from a negative to a positive phase also involved (Mohino et al. 2011). Marvel et al. (2020) underline, though, that unraveling the respective roles of aerosols forcing and oceanic variability is complicated since the two signals project onto each other.

While most, if not all, of the abovementioned studies focus on seasonal or annual totals, several recent studies point to a concomitant increase in heavy rainfalls in the region. Panthou et al. (2014) showed that, over the central Sahel, the proportion of rainy days considered as heavy and extreme (occurring less than 10 times and less than 2.5 times a year, respectively) in the total population of rainy days has increased substantially from the core of the drought to the recent period. In line with this, Taylor et al. (2017) conclude there is a threefold increase in the frequency of heavy storms affecting the whole Sahel. Furthermore, Chagnaud et al. (2022) reported that the strongest daily rainfalls experiment the largest increase in frequency. It is worth mentioning that the increase in rainfall extremes has likely been affecting the hydrology of the region over the second half of the twentieth century (Wilcox et al. 2018; Tramblay et al. 2020; Elagib et al. 2021), though other factors such as deforestation and land cover change might be involved (Descroix et al. 2018). Higher river outflows lead to more severe floods, causing an increase in damages and casualties (Di Baldassarre et al. 2010). At the other end of the hydroclimatic spectrum, extreme dry spells seem to show signs of an increase in frequency/duration, strongly affecting crop yields and freshwater availability (Porkka et al. 2021).

In fact, annual totals, on the one hand, and dry/wet extremes, on the other hand, have followed different trajectories

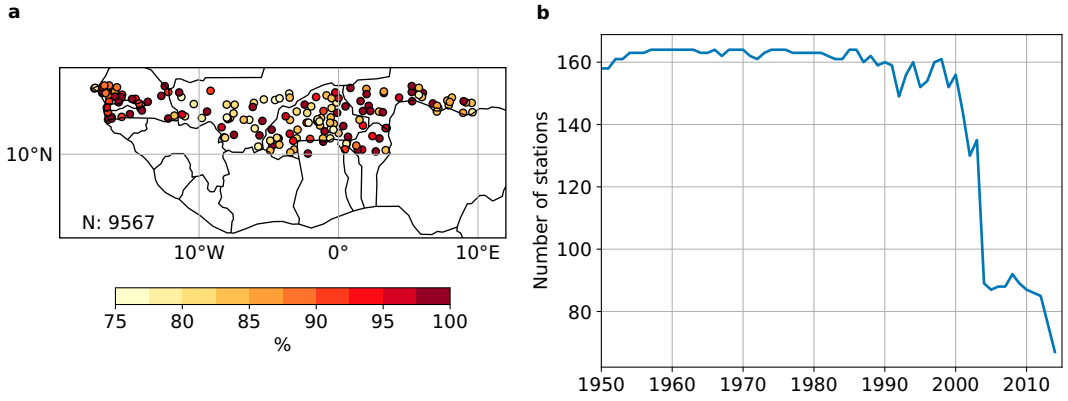

FIG. 1. (a) Rain gauge stations with a minimum of 75% of temporal coverage over the 1950–2014 period. The color shading corresponds to the proportion of valid years at each station (%). The *N* is the total number of observations (station-years). (b) Time series of the total number of stations over the domain.

over the past 65 years. While the 1950–80 drying trend originates primarily from a reduction in rainfall occurrences of about 25% (Le Barbé et al. 2002; Lebel and Ali 2009), the annual total improvement seems to result from a combination of increasing daily rainfall occurrences and intensities (Giannini et al. 2013; Panthou et al. 2018). However, while intensities have returned to their predrought level, occurrences remain well below their wet period level (Panthou et al. 2018). As a result, a larger contribution from heavy rainfall events to annual totals was reported by Panthou et al. (2014).

Precisely attributing the reasons of such contrasted evolution remains challenging since it is unclear how the Sahelian rainfall regime as a whole responds to various forcings. This raises the two fundamental questions addressed in this study: (i) Do climate models reproduce the observed rainfall regime evolution? and (ii) Can they provide some hints at attributing these signals?

Tackling the two aforementioned issues requires (i) reliable observational data at the daily resolution, here provided by an in situ rain gauge network, and (ii) climate model outputs from various types of simulation: coupled atmosphere–ocean global climate model (AOGCM) simulations with realistic and idealized forcings and atmosphere-only (AMIP) simulations. These latter simulations are especially relevant for analyzing rainfall regimes simulated by climate models in tropical regions, where SST patterns are of paramount importance. The data are described in section 2 together with the methodology. In section 3 an overview of the recent rainfall regime evolution, as captured by climate models and observations, is provided. Section 4 explores the large-scale drivers of the evolution, for the first time giving insights on how the rainfall regime in the Sahel responds to various forcing factors. Key results are discussed in section 5 and summarized in section 6.

2. Data and methods

a. Observational data

The Base de Données Pluviomètres (BADOPLU) database (e.g., Le Barbé et al. 2002; Lebel and Ali 2009; Panthou et al. 2018; Chagnaud et al. 2022) is used as a reference. This database gathers daily rain gauge data from national meteorological services of West African countries. Only stations with at least 75% of years flagged as valid over the 1950–2014 (65 years) period were selected (the quality-control procedure applied to remove outliers and other invalid data is thoroughly described in the supplementary material of Panthou et al. 2018). This sampling procedure leads to consider a set of 164 stations, for a total of 9567 station-years (over a maximum of $164 \times 65 = 10\,660$ station-years, Fig. 1a). The majority of missing station-years belong to the most recent period (Fig. 1b), linked to both the deterioration of the rain gauge networks and the growing difficulties in accessing rainfall data.

b. Model data

Models from phase 6 of the Climate Model Intercomparison Project (CMIP6; Eyring et al. 2016) are used in this study. More specifically, we need models having daily rainfall data available for at least one atmosphere-only (AMIP) simulation, a preindustrial control (PICTL) simulation and several realizations of the historical simulations with detection and attribution forcings (DAMIP; Gillett et al. 2016): natural-only (NAT, with solar irradiance and volcanic aerosols loading), aerosols-only (AER, with anthropogenic aerosols loading), greenhouse gases-only (GHG), and all forcings (ALL, natural plus anthropogenic). These rather stringent criteria led to selection of a subset of eight models (shown in bold text in Table 1) that does not allow us to sample the full range of CMIP6 models uncertainty; however, we find a similar behavior with another set of different CMIP6 models regarding rainfall metrics considered in this study (in ALL runs, Fig. S1 in the online supplemental material). The largest common number of members for DAMIP simulations is 2. We therefore use two members for each of the eight models to avoid overweighting the models with more members (see Table 1). For AMIP, we use the 10-member ensembles of CESM2, IPSL-CM6A-LR and MIROC6, with simulations starting in 1950, 1958, and 1979, respectively. For the other five models, only one AMIP realization is used, with simulations starting

TABLE 1. Model names, horizontal resolutions (° lat × ° lon), historical and DAMIP members used, AMIP members with period of the simulation, preindustrial control simulation length (years), and references. Models whose name is set bold are used in the main material, and the others are used to test the sensitivity of the results to the number of members.

Models	Horizontal resolution	Historical and DAMIP members	AMIP members	PICTL	References
ACCESS-ESM1-5	1.25 × 1.88	r1i1p1f1; r3i1p1f1	r1i1p1f1 (1979–2014)	900	Ziehn et al. (2020)
CESM2	0.94 × 1.25	r1i1p1f1; r3i1p1f1	r1-10i1p1f1 (1950–2014)	1200	Danabasoglu (2019)
CNRM-CM6-1	1.4 × 1.41	r1i1p1f2; r2i1p1f1	r1i1p1f2 (1979–2014)	500	Voldoire et al. (2019)
HadGEM3-GC31-LL	1.25 × 1.88	r1i1p1f3; r2i1p1f3	r1i1p1f3 (1979–2014)	500	Andrews et al. (2019)
INM-CM5-0	1.5 × 2.0	r1-10i1p1f1	—	1200	Volodin et al. (2017)
IPSL-CM6A-LR	1.27 × 2.5	r1i1p1f1; r2i1p1f1	r2-r11i1p1f1 (1958–2014)	1200	Boucher et al. (2020)
MIROC6	1.4 × 1.41	r1i1p1f1; r2i1p1f1	r1-10i1p1f1 10 (1979–2014)	600	Tatebe et al. (2019)
MPI-ESM1-2-LR	1.86 × 1.88	r1-10i1p1f1	—	1000	Mauritsen et al. (2019)
MRI-ESM2-0	1.12 × 1.12	r1i1p1f1; r2i1p1f1	r1i1p1f1 (1979–2014)	200	Yukimoto et al. (2019)
NorESM2-LM	1.89 × 2.5	r1i1p1f1; r2i1p1f1	r1i1p1f1 (1979–2014)	500	Seland et al. (2019)
UKESM1-0-LL	1.25 × 1.88	r1-4i1p1f2; r5-7i1p1f3; r8-10i1p1f2	—	1100	Sellar et al. (2019)

in 1979. For consistency, we use the same subset of models for the whole study.

Three other models are considered to form a subset of eight models (ACCESS-ESM1-5, CESM2, CNRM-CM6-1, INM-CM5-0, IPSL-CM61-LR, MIROC6, MPI-ESM1-2-LR, and UKESM1-0-LL) having at least 10 members with all historical forcings. This subset is used for evaluating the sensitivity of the analyses to the number of members.

Model data are kept to their native horizontal resolution for all the time series analyses in order to avoid data quality downgrading. Only for the spatial pattern analysis are model data regridded on a common 2° × 2° grid using a bilinear interpolation.

c. *Methodology*

1) RAINFALL REGIME INDICES

Standardized indices relative to annual totals, annual maxima of daily rainfall and rainy days intensity and occurrence are computed in order to compare models and observations in a consistent way (see appendix A for calculation details). Since we are interested in identifying the forced response in models, the indices are computed for each member before averaging across members and across models to remove part of the ICV (Räisänen 2001; Hawkins and Sutton 2009; Deser et al. 2012). Although the 8 × 2 realizations do not allow to completely remove ICV, the results are only slightly sensitive to ICV, as shown by the fact that randomly selecting members (for models with more than two members available) barely affects the results. The historical evolution has also been assessed using models with 10 members under ALL forcing and similar results were obtained.

2) WET DAY DEFINITION

A wet day threshold value (in mm day^{-1}) is defined for each model to discriminate between dry and wet days; this more realistic identification of a rain event—as compared to using a unique threshold for all models—might allow for a consistent comparison of simulated and observed daily rainfall statistics. We select the daily rainfall value that yields the regional mean number of wet days (considering rainy days throughout the year) best matching with observations over the 1980–2014 period (in a multimember average, see Fig. S2). Note that to account for instrumental uncertainty, a threshold of 1 mm is used for observations, removing less than 1% of the annual total. Table 2 shows that, depending on the model, between 8% and 17% of the total rainfall is removed when considering daily rainfall amounts above the threshold (except for the IPSL-CM6A-LR model, where 29% is removed, meaning that a large share of the total annual rainfall is produced by small daily rainfall amounts). Since the mean daily rainfall intensity of wet days displays a fairly homogeneous spatial pattern (no significant spatial variation, see Fig. S3), the intensity threshold value of each model is deemed constant over the whole region.

3) DRY AND WET EXTREMES ASSESSMENT

Assessment of extremes related to precipitation in the Sahel is sensitive to sampling effects, because of the high space–time variability of rainfall, mostly convective in this region (see e.g., Laurent et al. 1998). A statistical model

TABLE 2. Models wet day threshold (mm day^{-1}) and the proportion of annual total rainfall removed by applying the threshold (%).

Models	Wet day thresholds (mm day^{-1})	Annual rainfall removed (%)
ACCESS-ESM1-5	4.0	15.4
CESM2	4.0	14.2
CNRM-CM6-1	3.5	7.8
HadGEM3-GC31-LL	2.5	8.2
INM-CM5-0	2.5	12.5
IPSL-CM6A-LR	6.0	29.8
MIROC6	4.5	15.0
MPI-ESM1-2-LR	5.0	11.9
MRI-ESM2-0	4.5	15.5
NorESM2-LM	4.0	16.8
UKESM1-0-LL	2.5	8.2

based on a regional generalized extreme value (RGEV) distribution is used here to limit these sampling effects. This model allows for a consistent pooling of data into a single sample by accounting for the spatial gradients of extreme rainfall statistics, thus making the overall inference more robust (see details in appendix A).

Annual maxima of daily rainfall (AMAX) are used as a wet extreme metric. For dry extremes, annual maxima of the number of consecutive dry days (CDD) are considered; CDD series are computed on the June–September (JJAS) period i.e., the core of the rainy season in the Sahel. In both cases the RGEV model is fitted on running 20-yr time windows spanning the 1950–2014 period (a 20-yr period is assumed to be a good trade-off between inference robustness, by aggregating a large enough amount of data, and temporal resolution). For each 20-yr period, the T-yr return level at any point in space is derived [where T is the return period, see Eq. (A5)] and its change with respect to a baseline value is computed. As can be seen in Eq. (A5), a change in return level may arise from a change in any of the GEV parameters, or a combination thereof. As such, the return level provides a synthetic vision of the change in extreme value distribution, with the additional advantage to be more relevant from an end-user standpoint; it will thus be used throughout this study.

Additional to fitting a stationary RGEV model to running-window AMAX samples, use is made of a regional nonstationary GEV (RNSGEV) model wherein the location and scale parameters are expressed as a linear function of time (Chagnaud et al. 2022, see appendix B). To make the model inference (i.e., the trend estimation) more robust against ICV and sampling variance of the parameters, the RNSGEV model is fitted on a single regional AMAX sample gathering data from the two available members (for each model and experiment). The return level of any rarity at any point in space and any year may be derived from the RNSGEV model [Eq. (B2)], and the linear trend computed accordingly.

4) Rainfall response and significance assessment

The hypothesis of a possible trend in rainfall statistics is tested by looking at:

1) a nonparametric Theil–Sen slope estimate computed over a period for which a forced signal is expected; namely, the 1980–2014 period,
2) a difference between two distinct periods of a time average of the quantity of interest.

The two sources of uncertainty affecting the signal detection and attribution are due to (i) the role of ICV and (ii) different model formulations (structural uncertainty). Considering model ensembles allows sampling these uncertainties (see e.g., Lehner et al. 2020): for a given model, a multimember ensemble allows sampling ICV uncertainty while resorting to a multimodel ensemble allows accounting for structural uncertainty. For this latter issue, a multimember ensemble (for each model) is necessary in order to remove—at least partly—the influence of ICV when assessing the structural uncertainty. Comparing the signal produced by distinct models may be flawed by the fact that each model has its own (i) internal variability and (ii) sensitivity to forcings and thus its own signal-to-noise ratio. Here the use of standardized indices allows removing the effect of distinct model-simulated ICV and thus to compare the models on a common grounding. Addressing the model sensitivity issue is not within the scope of this study and, without any a priori knowledge that one of the selected models is especially unrealistic with respect to reproducing the Sahelian rainfall regime, we considered all models equally in a "one model, one vote" approach.

The significance of the identified response against the influence of each source of uncertainty is assessed in various ways. The multimodel, two-member 1980–2014 trends in ALL simulations are first compared to (i) ICV alone, as sampled in the PICTL simulations, and (ii) historical trends in NAT simulations. A Kruskal–Wallis test, whose null hypothesis is that the two samples are drawn from the same population without assuming a specific distribution or size of the compared samples, is used in this aim.

The significance of any detected trend in the regional mean daily rainfall intensity (I) and occurrence (N) signals is assessed against the null hypothesis of no change using a one sample, two-sided Student's t test: for each year, the samples of 8×2 I and N values are compared to 0, the expected value in the absence of forced signal.

For the spatial pattern analysis, the model uncertainty is accounted for by computing the intermodel agreement on the sign of the response, quantified as a difference between two distinct periods in the pointwise, time-average intensity and occurrence values. The response is assumed robust against model uncertainty when at least 75% (6 out of 8) of models (two-member average for each) agree on the sign of the difference.

3. Recent Sahelian rainfall reinforcement as seen by observations and climate models

a. *Annual totals and heavy rainfalls*

The evolution of the regional standardized indices (SI) for annual totals (ATOT) and daily rainfall annual maxima, computed from in situ observations (in black) and climate model outputs are shown in Fig. 2. Atmosphere-only model simulations (Figs. 2a,c) allow evaluating the capacity of climate models to capture the Sahelian rainfall response to SST patterns (since observed SSTs are used in these runs). In the CESM2 AMIP simulations, covering the full period of observation, the wet–dry transition of the 1950–80 period is well captured (Fig. 2a). This is also the case, yet to a lesser extent, with the IPSL-CM6A-LR model. This shows that the mechanisms linking SST patterns to Sahel rainfall are satisfactorily simulated, at least in these models.

Looking at various types of AOGCM simulations provides some clues on the factors that best account for the rainfall evolution observed over the past 65 years. While the magnitude of the mostly internally generated wet–dry transition is not expected to be fully reproduced in the AOGCM ensemble average, it is noteworthy that the ALL simulations capture a small part of the annual totals decreasing trend, attributed to anthropogenic aerosols loading (Biasutti and

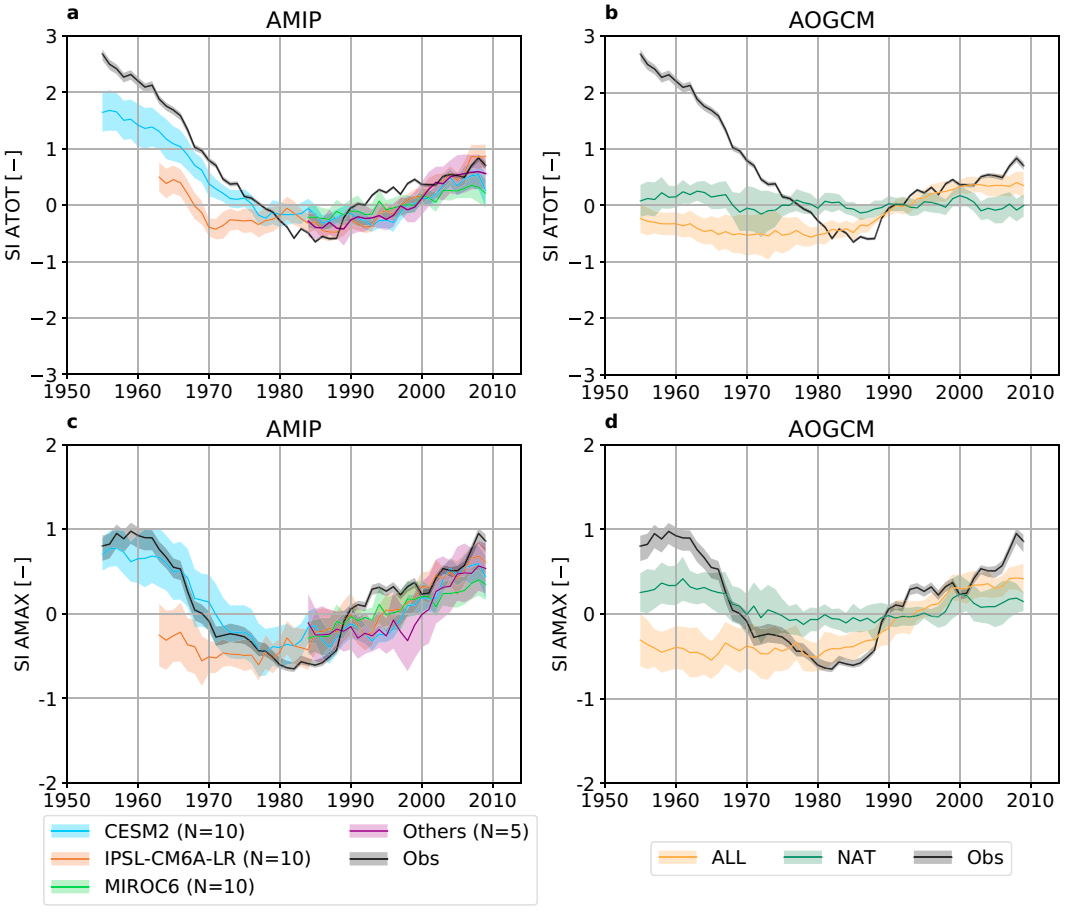

FIG. 2. (a)–(d) Standardized indices (SI) of annual total (ATOT) rainfall for (a) AMIP simulations and (b) AOGCM NAT (green) and ALL (orange) simulations. (c),(d) The SI of annual maxima daily rainfall (AMAX) from AMIP and AOGCM simulations, respectively. In (a) and (c), CESM2 (blue), IPSL-CM6A-LR (brown), and MIROC6 (green) are median and ±1 standard deviation (s.d.) across the 10-member ensembles covering the 1950–2014, 1958–2014, and 1979–2014 periods, respectively. The purple line and shading correspond to the median and ±1 s.d. across the single-member, five-model ensemble (see legend). Lines and shadings in (b) and (d) correspond to the median and ±1 s.d. across two-member multimodel ensembles. Note the different vertical axis scale for SI ATOT and SI AMAX. Observations are shown in black, with gray shading corresponding to the uncertainty due to network configuration. All time series are smoothed with a 11-yr running mean to emphasize the multidecadal evolution.

Giannini 2006; Ackerley et al. 2011). One may thus expect that this forcing influence is also captured when acting the other way, i.e., when aerosols concentrations decrease; Figs. 2b and 2d suggest it is indeed the case. However, the post-1980 forced increase seems to be of larger amplitude as compared to the 1950–80 decrease, suggesting a contribution from other external forcing factor(s). The respective share of natural and anthropogenic forcing factors is further explored in section 4.

Having in mind that AOGCMs may be biased in terms of SST patterns (see section 5b), comparing AOGCM and AMIP simulations sheds an additional light on the role of ocean-mediated internal variability with respect to that of external forcing factors. In this respect, a noticeable difference between AMIP and ALL simulations is the starting year of the rebound, which occurs about 10 years earlier in ALL runs. The observed signal (as captured by the rain gauges) therefore probably contains a forced component (as provided by averaging over AOGCM runs) since the early 1980s, counterbalanced by internal oceanic variability until the early 1990s (as shown by the AMIP simulations). The 1980–90 period is thus an illustrative example of how ICV and external forcings may have compensating effects at the decadal scale.

The post-1980 increase in extreme daily rainfall intensity is clearly visible in Fig. 2c, where the SI of the observed regional annual maximum daily rainfall (AMAX) has increased from a value of −0.5 in the early 1980s to almost +1.0 in the 2010s. Both the ALL (Fig. 2d) and AMIP (Fig. 2c) simulations are well capturing this trend, even though with a weaker amplitude. This is not the case for the NAT simulations, suggesting that anthropogenic forcings play a role in this surge of intense daily rainfall as well.

This issue is further explored by computing the 1980–2014 trends for the ATOT and AMAX indices in NAT and ALL

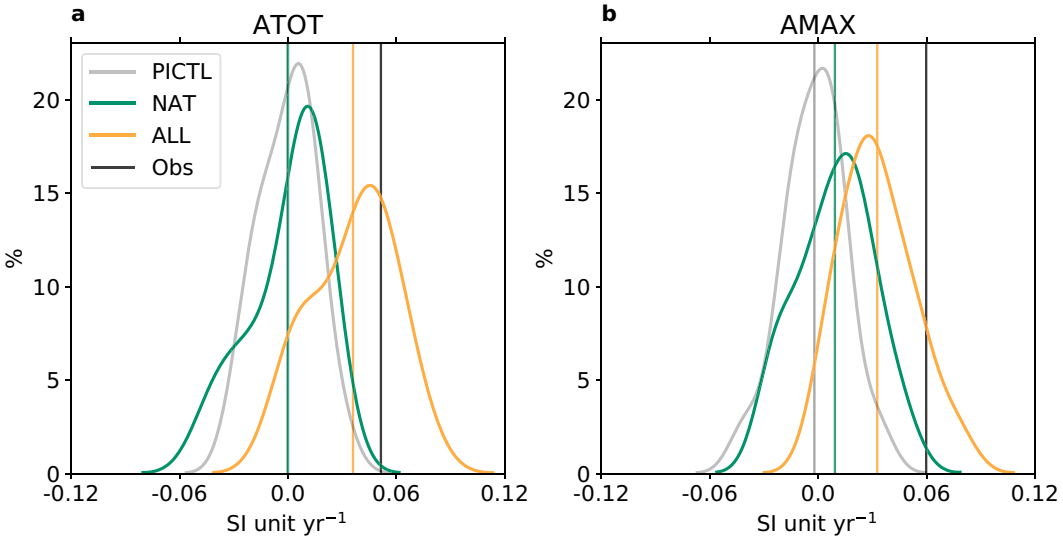

FIG. 3. Probability density functions (PDF) of the (a) SI ATOT and (b) SI AMAX linear trends (in SI unit yr^{-1}) computed over 1980–2014 for NAT (green) and ALL (orange) runs and on nonoverlapping 35-yr time periods randomly sampled in the preindustrial control (PICTL) simulations (gray). The means of the 16 trends computed for each type of simulation are displayed as vertical lines. The observed trend is indicated by the black vertical line.

simulations. The distributions of these two sets of 8 × 2 trend values are compared in Fig. 3 with the control-climate one, obtained by computing the trend on two randomly sampled, nonoverlapping 35-yr periods in each model's PICTL simulation. Since standardized indices are considered, all models trend values may be pooled into one sample (for each index and each experiment—ALL, NAT, and PICTL). For both ATOT and AMAX, the distribution of the NAT simulations (green) and of the PICTL simulations (gray) are not statistically different according to a Kruskal–Wallis test, with p values of 0.85 and 0.11, respectively, and a mean trend close to 0 (in SI unit yr^{-1}) in both cases. The ALL distributions (orange) are clearly shifted toward larger values and statistically different from the NAT and PICTL ones (p values < 0.01), with a mean trend of 0.04 and 0.03 for ATOT and AMAX, respectively (as compared to 0.05 and 0.06 for the observed ATOT and AMAX, respectively). Simulations incorporating anthropogenic forcing factors are thus the only ones able to detect the observed increasing trend of both annual totals and extreme daily rainfalls in the region. Similar conclusions are drawn when performing the same analysis on the larger samples (8 × 10) available for the ALL and PICTL simulations only (see Table 1), showing the robustness of our findings against ICV and model uncertainty (Fig. S4).

b. *Rainfall regime intensification in CMIP6 historical simulations*

Basically, the regimes of the annual totals and extremes are controlled by two key variables: the number of occurrences and the intensity of rainy days. In the following we thus explore how the evolution of these two variables compare to the evolution of ATOT and AMAX. For this purpose, we compute standardized indices, I and N, whose time evolution is displayed in Fig. 4 for the AOGCM and AMIP simulations. In ALL, the trends for both I and N are quite consistent with the observations after 1990, while notable differences are seen before 1990 (Figs. 4b,d); this is, again, because the pre-1990 I and N evolution mainly arises from ICV, as confirmed with the CESM2 AMIP simulations (Figs. 4a,c, blue line and shading).

It is noteworthy that prescribing observed SST values brings a larger improvement for N than for I, as can be seen when comparing both the spread among models and the match with observations in Figs. 4a and 4c. This shows that SSTs exert a stronger control on the model-simulated daily rainfall occurrences, as reported by Giannini et al. (2013) and Salack et al. (2014) for observations. On the other hand, intensity may be more closely related to local processes, possibly involving interactions with the ground surface and therefore less constrained by SSTs, which would explain the larger intermodel spread.

How different from 0 are the forced (multimodel/multimember mean) regional intensity and occurrence standardized values is quantified with a one sample, two-sided Student's t test [see section 2c(4)]. It is clear from Fig. 5, showing the p value of the test for each year, that here again the rainfall regime evolution is largely due to large-scale anthropogenic factors: the p values are smaller than 1% most of the time in ALL, except around the center of the reference period used for standardization (1979–2008). In NAT, the p values are generally above 5%, meaning that the null hypothesis of no change may not be rejected at this risk level.

c. *Dry and wet extreme return levels evolution*

A regional GEV distribution is used here to model CDD and AMAX time series on moving 20-yr time windows, allowing to compute the 10-yr return levels for characterizing dry and wet extremes evolution [see section 2c(3)]. In

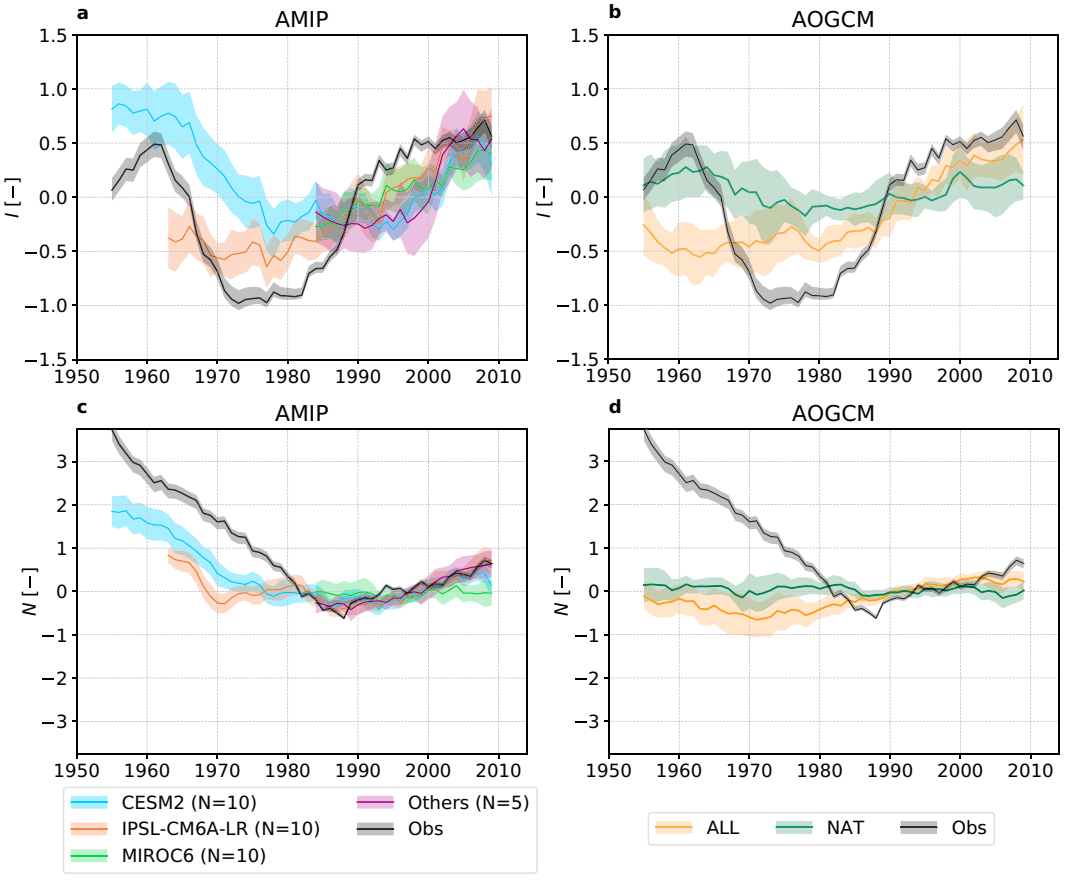

FIG. 4. Standardized indices of the regional mean daily rainfall intensity (I) in (a) AMIP and (b) AOGCM simulations, and of the regional mean number of wet days (N) in (c) AMIP and (d) AOGCM simulations. Line and shading colors are as in Fig. 2. All time series are smoothed with a 11-yr running mean to emphasize decadal variability.

observations, dry extremes show a persistent increase from 1960 to 2000 and a plateau afterward (black curve in Fig. 6a). In spite of this fairly homogeneous increase, the N evolution (black curve in Figs. 4c,d) leads to distinguish two distinct periods. As expected, the systematic decline in N from 1950 to the mid-1980s has produced an enhancement of the dry spell lengths (Le Barbé et al. 2002). Afterward, the occurrence increase is associated with an increase in I (Fig. 4a); because stronger—and potentially larger (e.g., Prein et al. 2017; Lochbihler et al. 2019)—storms tend to remove more moisture

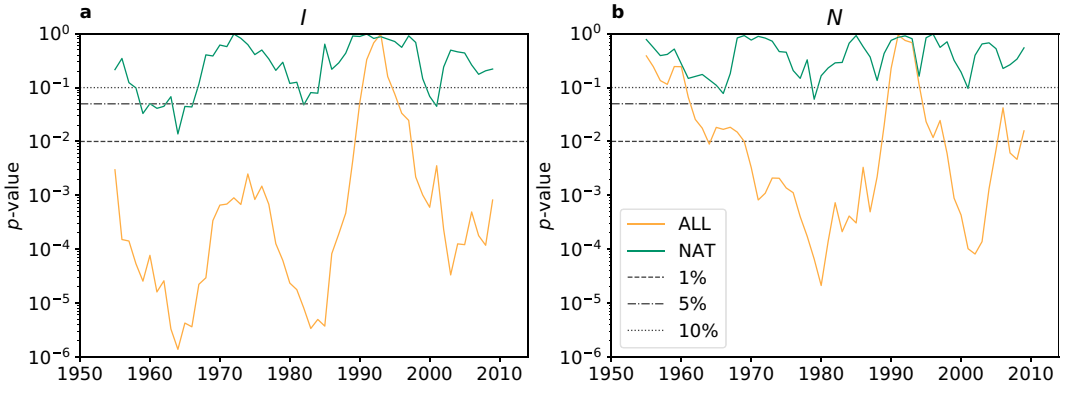

FIG. 5. The p value of a one-sample, two-sided Student's t test comparing, for each year, the mean across members of the (a) I and (b) N values to 0, for ALL (orange) and NAT (green) simulations. Thresholds for the p value of 1%, 5%, and 10% are shown with dashed, dashed–dotted, and dotted lines, respectively.

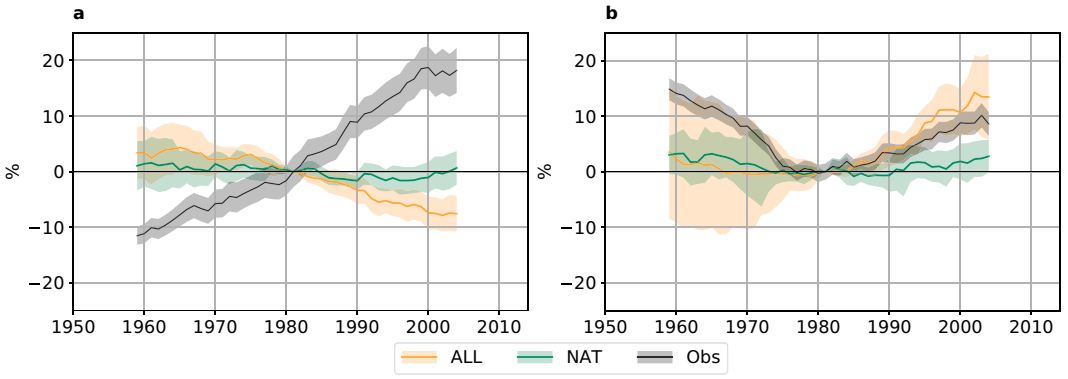

FIG. 6. Change in the 10-yr return level of (a) dry spell length and (b) daily rainfall relative to the 1972–91 baseline value (%) for 20-yr moving windows spanning the 1950–2014 period. The orange line and shading are the median and ±1 s.d. across multimodel two-member ensemble medians. Black line and gray shading correspond to the observed values and associated uncertainty due to network configuration.

from the atmosphere, this might as well have favored longer inter-event durations (Trenberth 2011). The slight levelling-off of I after 2000 would thus explain the observed CDD plateau. In models, CDD remains stable during the first period, likely because most of the occurrence decline was internally generated and therefore not present when averaging across multiple AOGCM realizations. The recent period, however, gives an illustrative example that robustness does not imply realism, with none of the models capturing the increasing trend in extreme dry spell length. This conclusion proves to be hardly sensitive to the wet day threshold value (Fig. S5a) and points to an intrinsic deficiency of models, as further discussed in section 5d.

Wet extremes tell a different story: the pattern of change in daily rainfall 10-yr return level is in overall agreement with that of AMAX depicted in Fig. 2d, with a signal mostly flat prior to 1980 and an increasing trend starting at the turn of the 1980s (Fig. 6b). Note that whereas the model-simulated SI AMAX remains lower than the observed one (Fig. 2d), the 10-yr return level is most of the time overestimated; this is because some models simulate a larger increase in the scale parameter of the regional GEV distribution, which more strongly affects the strongest (or rarest) events, a feature not captured by the SI. Also worth mentioning is the larger spread among members prior to 1980 with, interestingly, some members capturing the magnitude of the strong decreasing trend in extremes, of −15% in 20 years. The larger intermodel agreement after 1980 indicates that this signal is at least partly externally forced, while the almost flat signal in NAT supports the anthropogenic origin of this rainfall intensification.

4. Mechanisms for rainfall regime changes of the last decades

In the previous section, CMIP6 models have been shown to capture the observed evolution of key parameters of the Sahelian rainfall regime; namely, the annual totals, the extreme daily rainfalls, the mean intensity, and the mean annual number of rainy days. Moreover, an unequivocal influence of anthropogenic forcing factors on these evolutions has been highlighted. Building on these two aspects and because one may expect the intensity and frequency to respond to different factors in different ways, this section delves into the respective roles of external factors on the recent rainfall regime evolution.

a. *Intensity and occurrence*

To assess more finely how internal variability and external factors may have contributed to triggering the new rainfall regime that has been taking shape since the mid-1980s, it is worth looking at the spatial patterns of changes in intensity and occurrence. To filter out the large interannual variability at the GCM mesh scale, the time evolution of the rainfall regime is characterized by computing the differences of I and N averaged over two 30-yr periods (1950–79 and 1985–2014) for ALL and NAT-, AER-, and GHG-only simulations, using the same subset of two-member ensembles as previously.

For intensities, the ALL simulations display a widespread increase, with large model agreement (6 models out of 8 agree over 73% of the Sahel domain, Fig. 7a). Aerosols and GHG effects combine well to explain this overall pattern of evolution, albeit with different spatial patterns when looking at each of these two factors separately. Aerosols drive a widespread intensity increase, with good model agreement (75% of the models agree on the sign of change over one-half of the domain, Fig. 7e). GHG runs display a strong intensity increase in the easternmost part of the Sahel (Fig. 7g). A dipole structure of the mean rainfall response to increasing GHG concentrations is a robust feature of future projections in the Sahel, with a wetter east and a drier west (Fontaine et al. 2011; Monerie et al. 2012). It has been suggested that a reinforcement/displacement of the Saharan heat low could drive a stronger moisture convergence over the eastern Sahel (ES), an enhanced southwesterly flow adding up to the purely thermodynamical effect of an increased atmospheric moisture holding capacity, as suggested by observations (Evan et al. 2015; Lavaysse et al. 2016) and climate models (Gaetani et al. 2017; Monerie et al. 2021). Over western Sahel (WS), ALL

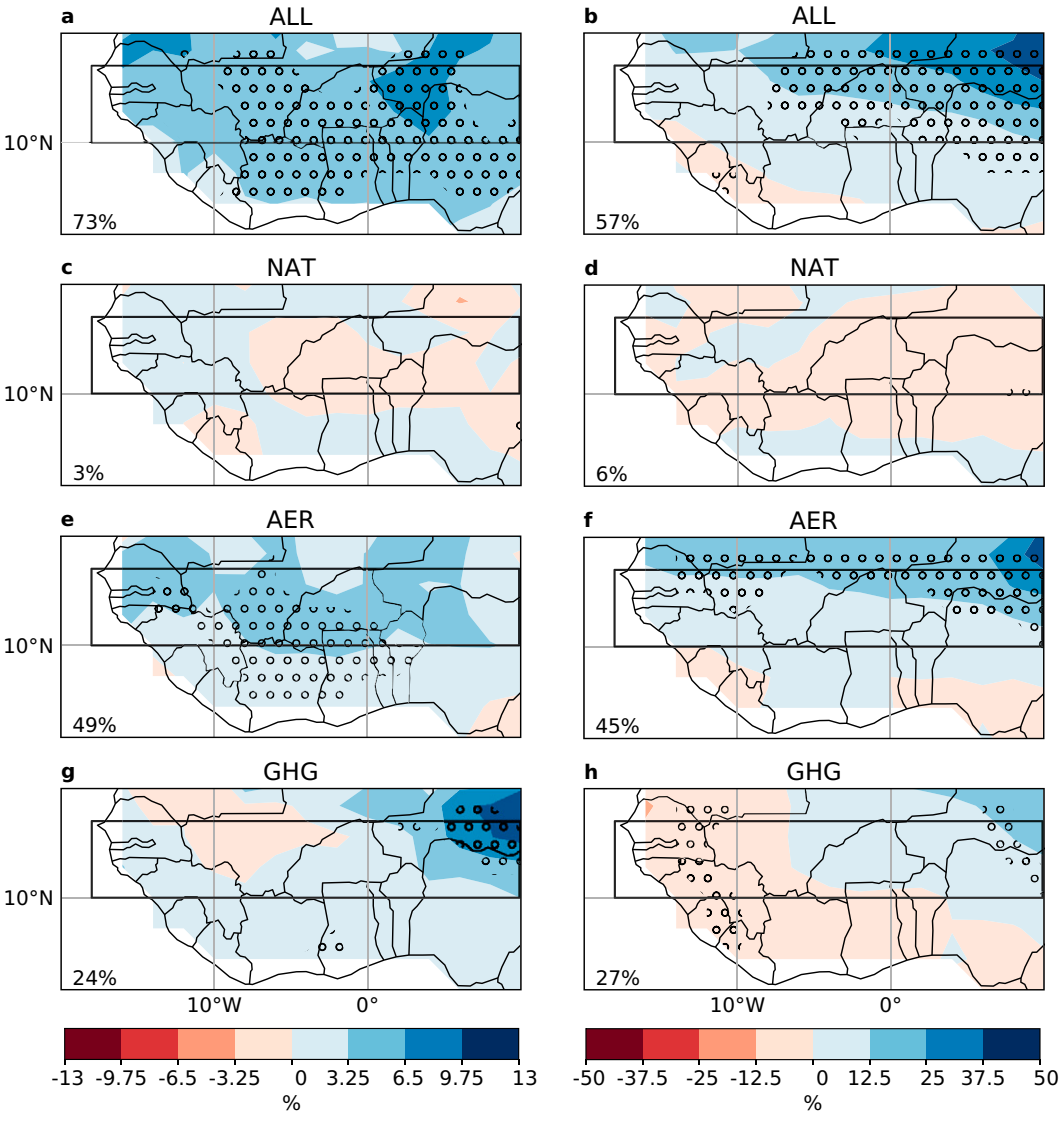

FIG. 7. Multimodel mean of (left) intensity and (right) occurrence relative change (%) between 1985–2014 and 1950–79 in (a),(b) ALL, (c),(d) NAT, (e),(f) AER, and (g),(h) GHG AOGCM experiments. Stippling indicates grid cells where 6 out of the 8 models agree on the sign of change. Note the different color scales for *I* and *N*. Boxes correspond to the Sahel region used in this study (10°–15°N, 20°W–10°E). Numbers in the bottom-left corner stand for the proportion of grid cells meeting the model agreement criterion within the Sahel box.

runs well capture the intensity evolution as a result of the AER and GHG effects (Figs. 8a,e,g). The larger spread in AMIP runs over WS confirms the limited SST influence on intensity, even in this coastal region (Fig. 8i).

Regarding occurrences, the southwest–northeast gradient of the occurrence evolution in ALL is an obvious superimposition of the AER and GHG fields (Figs. 7b,f,h). The latitudinal gradient in AER runs likely reflects a further north migration of the ITCZ rainband in response to the reduction in aerosols emissions (Rotstayn and Lohmann 2002; Chang et al. 2011) with, in absolute terms, an additional ~2 rainy days per year over the whole region between the two considered periods (not shown). The occurrence evolution in ALL is slightly underestimated over WS (Fig. 9a) while it is in much better agreement in AMIP runs (Fig. 9i). This suggests that an internally generated mode of SST variability might have counteracted the drying effect of GHG depicted in Fig. 7h, though this discrepancy may also arise from a deficiency of AOGCMs to capture the correct SST trend. The opposite holds over ES, where the increase of occurrences is slightly overestimated in ALL because of the combined effect of aerosols and greenhouse gases forcing (Figs. 9b,f,h). In AMIP runs the occurrence increase over ES is slightly leveled-off (Fig. 9j). The larger intermodel spread (as compared to that over WS) is likely due to the more remote oceanic influence in this area.

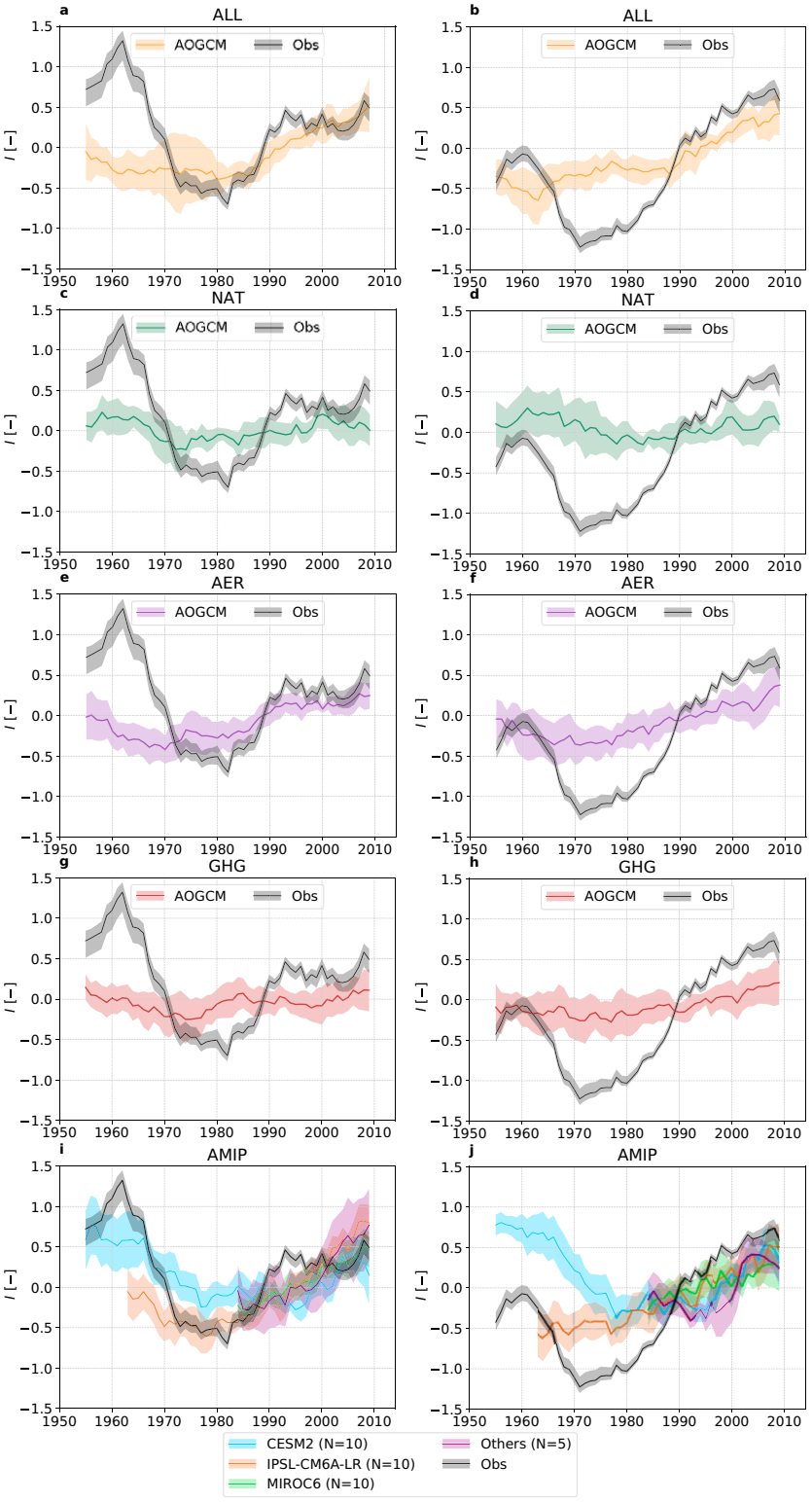

FIG. 8. Standardized indices of regional mean intensity (I) for (left) western and (right) eastern Sahel. Multimodel medians and ±1 s.d. of two-member ensemble medians are shown with color line and shading, respectively. Observations are shown in black. All time series are smoothed with a 11-yr running mean to emphasize decadal variability.

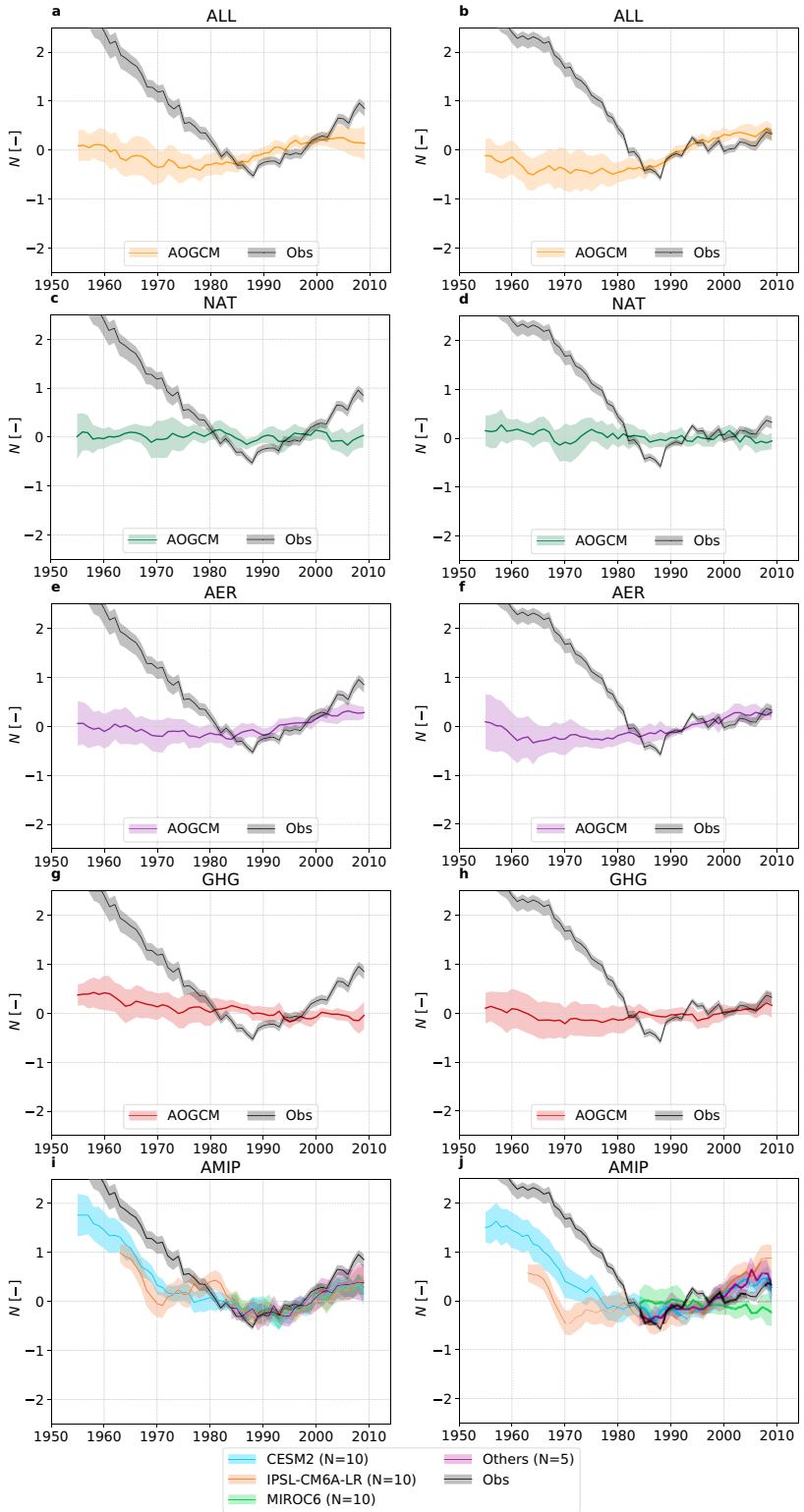

FIG. 9. As in Fig. 8, but for the regional mean occurrence (N).

Another noteworthy feature is the dipole pattern shown in Fig. 7h, with a substantial occurrence reduction over WS while occurrence increases over ES, with good model agreement. Thus, the well-documented Sahelian dipole turns out to be a combined effect of intensity increase over the ES and occurrence shrinking over the WS under GHG forcing (see Figs. 8h, 9g, respectively). Interestingly, these two features are fairly robust across models, in spite of the relatively limited GHG forcing strength of the historical period. In addition, using the idealized experiment wherein CO_2 concentration exponentially increases at a rate of 1% yr^{-1} starting from a preindustrial control state (1pctCO_2), the dipole-like structure of I and N evolution turns out to be monotonous (not shown). Thus, were the GHG emissions to continue in the coming decades, one may not exclude this occurrence–intensity dipole to strengthen. This would lead to further rainfall intensification, keeping in mind that ICV may either damp or amplify this forced signal on interannual to decadal time scales.

b. *Recent wet extremes trend*

Based on the use of a regional GEV model it was shown in section 3 that the ALL simulations realistically reproduce the intensification trend of wet extremes seen in observations from 1980 to 2014 (Figs. 2d, 6b). We will look below at this evolution in single-forcing simulations, using a nonstationary regional GEV model wherein both the location and the scale parameters vary linearly with time over the 1980–2014 period (see appendix B for details).

For each model's two-member ensemble we derive the 10-yr return level trend. Figure 10a shows that over the whole Sahel, the median trend across models in ALL (5.43% $decade^{-1}$) matches strikingly well with the observed value of 5.29% $decade^{-1}$ [(4.2–6.2) 50% confidence interval, black line and gray shading], though with a relatively large intermodel spread (from 2.7% to 13.8% $decade^{-1}$). Aerosols contribute the largest share of this trend (3.7% $decade^{-1}$) with a narrow spread (1.7%–6.1% $decade^{-1}$), consistent with the good model agreement shown in Figs. 7e and 7f. GHG runs have a positive median trend (1.8% $decade^{-1}$) affected by a large intermodel spread (from −4.1% to 6.3% $decade^{-1}$), largely explaining the spread seen in ALL: the IPSL-CM6A-LR model produces the largest trends in ALL (13.8% $decade^{-1}$) and GHG (6.3% $decade^{-1}$) runs, whereas the CESM2 model has the second smallest trend in ALL (3.0% $decade^{-1}$) and a largely negative trend in GHG (−4.1% $decade^{-1}$). This regional behavior also applies at the subregional scales, as depicted in Figs. 10b and 10c for the Western and Eastern Sahel, respectively. Moreover, it shows some consistency with the spatial pattern analysis presented in section 4a (Figs. 8, 9): over WS, there is a gap of 1.4% $decade^{-1}$ between the observed and ALL simulation trends, likely resulting from the larger ICV influence over this area. Over ES, the NAT trend is slightly larger and with no negative trend. The larger signal in GHG over ES results from the large intensity increase (Fig. 8h); the large spread suggests that extreme rainfall events are especially sensitive to model formulation, as discussed in section 5c.

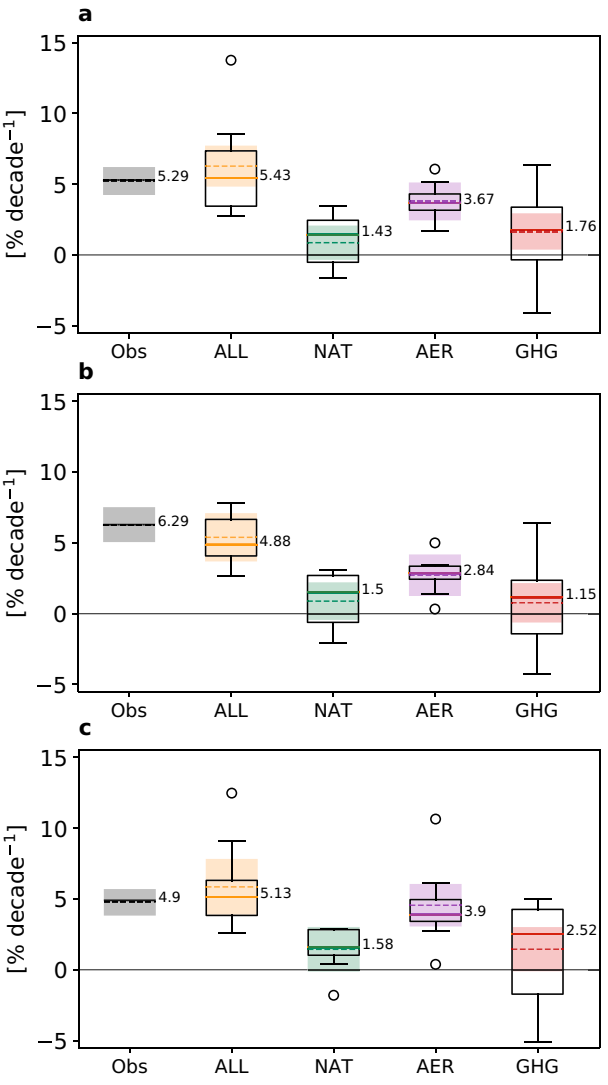

FIG. 10. The 1980–2014 trends of the daily rainfall 10-yr return level (% $decade^{-1}$) derived from the RNSGEV model fitted on two-member samples of annual maxima daily rainfall for each model over (a) the whole Sahel, (b) western Sahel, and (c) eastern Sahel. Boxplot diagrams show the intermodel spread for ALL, NAT-, AER-, and GHG-only simulations: box is the first (Q1)–third (Q3) interquartile range (IQR), whiskers extend from Q1 − 1.5 × IQR to Q3 + 1.5 × IQR. The median trend across models is indicated with the plain line and number aside. Shading depicts the uncertainty due to RNSGEV model inference for observations (gray) and models (color). Dashed lines indicate the median across 200 bootstrapped trend values.

5. Discussion

Our qualitative attribution analysis of the rainfall regime evolution in the Sahel leads us to conclude that anthropogenic forcing factors have played a significant role in driving the recent rainfall intensification trend. At the same time, the Sahelian rainfall is characterized by a strong decadal variability, largely associated with the SST patterns in various oceanic

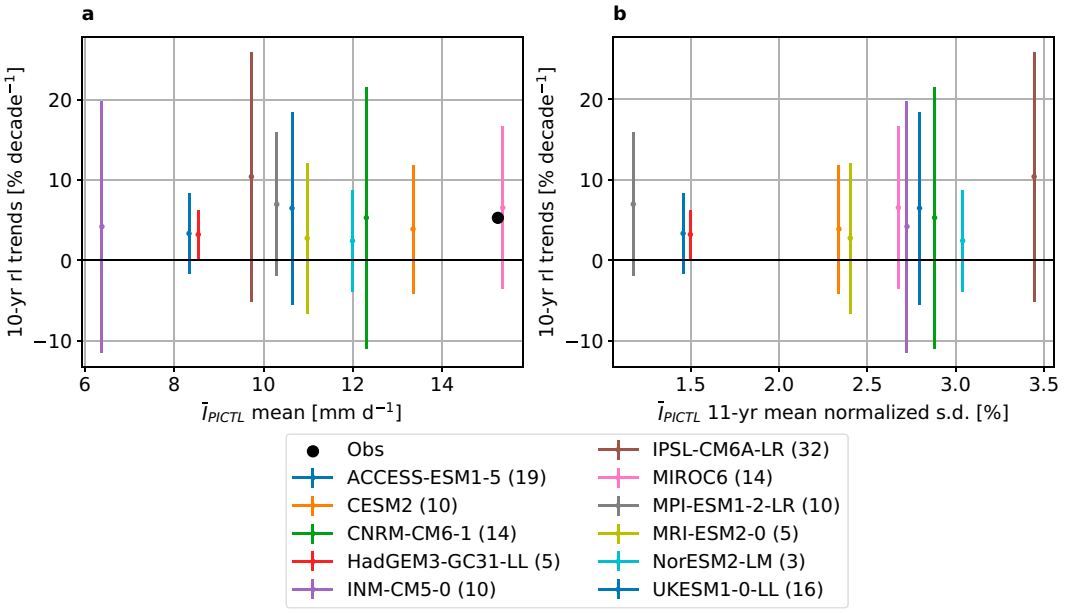

FIG. 11. The 1980–2014 10-yr return level trends in ALL simulations as a function of model's daily rainfall characteristics from the PICTL simulation. (a) The horizontal axis is the regional mean daily rainfall intensity (I; mm day^{-1}) averaged across $n \times 35$ years where n is the available number of members or 35-yr PICTL time slices, for each model (the smallest is chosen, see legend). (b) The horizontal axis is the standard deviation of the 11-yr running mean I time series, normalized by the mean I (%). The vertical lines correspond to the spread across the n trend values. The observed value is shown with a black dot in (a).

basins. Climate model biases in reproducing important features of oceanic spatial and temporal variability are known to be especially strong. One may thus wonder to which extent these biases may impair our confidence in the rainfall regime evolution produced by these models regarding both the past and the future. In this section the discussion first bears on the capacity of GCMs to capture the rainfall evolution over a specific region, a major advance of this study. Second, we discuss whether this finding could arise for wrong reasons (typically through compensating effects). Building on the assumption that models are indeed behaving correctly for the right reasons, we discuss the attribution of this evolution to anthropogenic forcing factors. The caveat previously highlighted regarding the incapacity of models to capture the evolution of extreme dry sequences leaves room for future research, as finally discussed.

a. Evolution of rainfall values

Whether considering annual totals, maximum annual rainfall or mean daily rainfall, AMIP simulations well capture the decline of the 1950–85 period (in the CESM2 model and to a lesser extent in the IPSL-CM6A-LR model), providing confidence in the capacity of climate models to correctly apprehend the WAM sensitivity to SST patterns. The post-1985 rebound of annual rainfall, associated with higher maximum annual and mean daily rainfall is also well captured (Figs. 2, 4). This means that despite their different structures, the various GCMs used in this study detect the proper amplitude of the recent intensification with respect to the 1950–85 decline, as soon as they are forced by the observed SST and sea ice cover values. More specifically, they correctly diagnose an annual mean rainfall that remains below the 1950s high, a maximum annual daily rainfall that is in the same order as in the 1950s and a mean daily rainfall that is now higher than in the 1950s. This latter point deserves some attention. Relative to the rainfall regime that prevailed over the 1950–70 period, there is a stronger increase of the mean daily rainfall than of the maximum annual daily rainfall and this is due to a persisting deficit of rainfall occurrences. The fact that GCMs are able to capture this fundamental feature of the Sahelian rainfall regime evolution provides some confidence for carrying out impact studies and planning adaptation strategies, keeping in mind that the decadal variability is interfering with long term trends in producing the actual pattern of evolution. In this respect, one may infer that the difference in timing and amplitude of the post-1985 intensification between AOGCMs and AMIP simulations represents the effect of the internal variability, and more specifically—for that particular period—the rebound from the unprecedented drought of the 1970s and 1980s: AMIP simulations combine the two effects while the AOGCMs ensemble average illustrates the forced evolution. Given the requirements for this type of study, only a limited number of models could be used. However, as can be seen from Fig. 11, the models used in this study have substantially different control climates, which seems to indicate that the detected trends stem from a robust regional climatic signal.

b. *Could the detected trends arise from compensating biases?*

This section addresses the issue of whether—and the extent to which—climate model biases in representing internal modes of climate variability and sensitivity to forcing factors may affect the conclusions of this study. In fact, compensating effects between these two types of deficiencies have the potential to yield good results for the wrong reasons, thus leading to draw incorrect conclusions. This issue also has implications for decadal predictability as well as century-long projections.

1) BIASES IN ICV

One major concern for the purpose and conclusions of this study is the difficulty of models for capturing the spatial and time patterns of SSTs, especially their decadal modes of variability, with such biases documented in CMIP3 and CMIP5 models (e.g., Mohino et al. 2016; Yan et al. 2018; Wills et al. 2019). Although a comprehensive evaluation of CMIP6 models is not available to date, the simulation of Atlantic multidecadal variability seems to be improved in several state-of-the-art AOGCMs, such as the CNRM (Voldoire et al. 2019) and IPSL (Boucher et al. 2020; Bonnet et al. 2021) models used here. Also of interest is the capacity of models for capturing the climate impacts of such modes of variability, which have been shown to differ substantially among a set of CMIP6 models by Hodson et al. (2022).

Both features—Atlantic decadal variability and its climate impacts—may be closely related to model biases in the oceanic mean state and the associated mechanisms (including coupling with the atmosphere), as documented in CMIP5 (Richter and Xie 2008; Richter et al. 2014; Rodríguez-Fonseca et al. 2015, among others) and CMIP6 (Richter and Tokinaga 2020) models, this latter study reporting only slight improvements in CMIP6 models. We note that model biases in various regions may affect the overall model behavior in different ways: decadal-scale variability primarily originates in northern North Atlantic (Wills et al. 2019) while Sahel rainfall variability and change is mainly ruled by tropical Atlantic SSTs.

Understanding how these various sources of error interact and (may) change with changing external forcings is essential to increase confidence in attribution and projection studies.

2) BIASES IN SENSITIVITY TO EXTERNAL FORCINGS

Another important aspect has to do with the sensitivity of model-simulated SSTs to different external forcing agents, especially GHG and aerosols. Regarding GHG-driven global warming (GW), Mohino et al. (2016) show, using one GCM, that the pattern of Sahel rainfall response to GW is not correctly simulated, mainly because of an incorrect tropical Atlantic warming trend (a finding in line with Shin and Sardeshmukh 2011). For aerosols, Menary et al. (2020) find that CMIP6 models have a larger sensitivity to changes in atmospheric aerosols loading as compared to CMIP5 models, mainly due to the indirect aerosols effect being now widely accounted for. This (possibly overestimated) sensitivity may well overwhelm an underestimated response to GHG forcing and/or a too weak decadal variability; this would lead to overly attribute the recent intensification to aerosols at the expense of other factor(s).

Notwithstanding these limitations, there are at least two reasons that support our conclusions that external forcing factors had an indisputable influence in shaping a significant evolution of the Sahelian rainfall regime since 1990. First, several previous studies have reported the implication of various forcing factors in the recent rainfall rebound (Dong and Sutton 2015; Giannini and Kaplan 2019; Marvel et al. 2020), even though noting that model underestimation of decadal-scale SST variability may reduce the spread about the estimated forced trend, leading to an overestimated signal-to-noise ratio. Second, working in a multimodel framework reduces the possibility of being correct for the wrong reasons.

c. *Attribution*

Assuming AOGCM simulations to be mostly influenced by the modification of the external forcing factors combination leads to assess whether one can disentangle the influence of the two main factors, aerosols and GHG concentrations. To that end, CMIP6-DAMIP simulations (Gillett et al. 2016) were used. Several authors consider that the unusual SST pattern of the Atlantic Ocean having caused the severe 1970–90 drought originates in the aerosol atmospheric content peaking in the 1970s in the Northern Hemisphere, before declining as a consequence of the regulations imposed since (see Hoesly et al. 2018). A significant share of the post-1985 evolution could thus be associated with this decline of the aerosol content, a hypothesis confirmed by our analysis showing that aerosols-only simulations display a more consistent and robust pattern of the post-1985 evolution (Fig. 7), and account for the largest share of the recent intensification trend of daily rainfall extremes (Fig. 10). The aerosols-only runs reproduce especially well the mean daily rainfall increase over the western halve of our study domain (Fig. 8e). By contrast, the GHG signal is weaker even though clearly present over the eastern Sahel. The spread of the 1980–2014 extreme rainfall trends produced by GHG simulations is likely linked to this GHG signal still being relatively weak in the first 15 years of the century. This emergence issue was difficult to address here given the small number of available GHG-only simulations. Dispersion between models may also be rooted in the manifold nature of the WAM response to global warming (e.g., Giannini 2010; Gaetani et al. 2017; Fitzpatrick et al. 2020; Chagnaud et al. 2020), making the simulations markedly sensitive to differences between models in representing one or several key mechanisms, especially those controlling scale interactions—for instance between regional climate dynamics and convection [model structural differences have been shown to account for a large share of the total uncertainty in future projections of regional precipitation (Hawkins and Sutton 2011), especially for monsoonal rainfall extremes (Zhou et al. 2020)]. However, since the GHG signal is expected to become more and more dominant, future sets of simulations incorporating the most recent GHG concentrations could display

smaller relative spreads and provide more confidence in end-of-the-century projections. Meanwhile, there is already sufficient evidence of the capacity of the current generation of climate models to attribute part of the ongoing Sahelian rainfall intensification to the GHG concentrations increase so as to take it into account in adaptation policies.

d. *Evolution of rainfall occurrences*

This paper has addressed the intensification issue in its broad sense, that is, evolving rainfall intensities and occurrences as reported in observations by Salack et al. (2016) and Panthou et al. (2018). However, while climate models convincingly detect the increase of mean rainfall intensities and extreme rainfall, the picture is somewhat bleaker for rainfall occurrences and the associated intraseasonal variability that largely controls water runoff and crop yields. On the one hand, the overall regional increase of the mean number of rainy days per year since the end of the 1980s is well detected by AOGCMs (Fig. 4d) as well as by AMIP (Fig. 4c) simulations. The latter also perfectly capture the fact that the mean occurrence rate remains much smaller than in the 1950s. This occurrence rate rebound seems mostly driven by the evolution of the aerosols forcing, while GHG-content increase entails an occurrence rate increase in the northeastern Sahel and a decrease elsewhere—especially significant over Senegal (Figs. 7h, 9g). On the other hand, when looking at extreme dry spell length, GCM simulations fail to capture the strong increase detected in observations (Fig. 6a). In other words, in nature, the mean number of rainy events has increased over the last decades but the probability of getting an unusually long dry spell has also increased, meaning a changing intraseasonal distribution of rain occurrences; in climate models the mean number of rainy events also increases but the distortion of the intraseasonal distribution is not seen. There are at least two factors that may explain this flaw: the first one is related to models while the second concerns the way extreme dry spells are statistically dealt with. From their analysis of in situ daily rainfall data in Senegal and Niger, Salack et al. (2014) evidenced the instrumental role of global SST anomaly patterns in conditioning the frequency of Sahelian dry spells. One may then think of a specific SST pattern causing the observed dry extremes trend not captured by the models. However, performing the CDD analysis on AMIP runs brings very little improvement (Fig. S5b), rather pointing to an intrinsic model deficiency. Supporting this, the recent study of Berthou et al. (2019), based on a convection-permitting model simulation, suggests that the tendency of GCMs to overestimate rainfall frequency—owing to the parameterization of convection (on this issue see e.g., Hagos et al. 2021)—is responsible for this flaw, thus pointing to an irreducible deficiency in this particular respect. Another set of factors to have in mind when comparing extreme dry spell length in observations and in models relates to statistical considerations and more specifically to the choice of the diagnostic variable and of the statistical metrics. First, the range of variation of the dry spell length is not so large, making the longest dry spell in a year not so good a diagnostic variable. Assessing the number of dry spells over a given critical threshold might be statistically more significant as well as more relevant in terms of impact on crop yields, for instance. Second, using a GEV-based model for representing the statistical distribution of extreme values associated with a discrete variable is questionable. It appears that a more specific and in-depth study should be carried out on the issue of the evolution of extreme dry spells in a context of increasing GHG concentrations.

6. Conclusions

The Sahel has been experiencing large rainfall fluctuations since the middle of the twentieth century, with two dominant sequences: (i) from 1950 to the end of the 1980s, a 20-yr wet period followed by a 20-yr widespread and intense drought; (ii) since the early 1990s, a partial recovery of the annual rainfall associated with an overall intensification of the rainfall regime. While rainfall intensification is an expected outcome of global warming, other factors may have a substantial influence, most notably the strong internal variability of monsoon climates, heavily influenced by SST pattern oscillations. An array of fully coupled and atmosphere-only state-of-the-art climate model simulations are used here to investigate whether they can help deciphering the various factors at play. Analyzing four regional rainfall indicators—the annual total rainfall, the mean daily rainfall intensity, the mean number of rainy days per year and the annual maximum daily rainfall—leads to the following conclusions:

- The intensification of the last 30 years is seen in both AOGCM and AMIP simulations, with the AMIP signal being closer to the observed one. This tends to establish that this intensification is partly driven by external forcing modifications (corresponding to the component seen by the AOGCMs) associated with the internal variability of the West African monsoon.
- Comparing the response of aerosols-only and GHG-only AOGCM simulations indicates that a notable part of the intensification—averaged over the last 30 years—was mainly driven by a decreasing atmospheric aerosols content starting at the end of the 1970s, whether due to an indirect effect on the monsoon dynamics through their influence on SST patterns or to a more direct/local effect.
- Looking at regional patterns allows us to further refine these conclusions. The continuing increasing trend of the mean daily rainfall in the east of the study domain is seen in both aerosols-only and GHG-only simulations, indicating they both play a role; by contrast, GHG-only simulations fail to capture the more complex signal observed in the west, indicating a prominent role of the aerosols there, probably through their influence on SSTs. The same qualitative result hold for the occurrences, with a GHG signal capturing much better the observed signal in the east than in the west. It may thus be inferred that the increasing GHG atmospheric content is a dominant forcing of the observed intensification in the eastern Sahel.
- While the climate simulations used here capture reasonably well the time–space evolution of the rainfall occurrences over the last 30 years, they do not correctly reproduce the observed trend of longer extreme dry spells. There is room for further

work on this issue, if only to refine the metrics and statistical approaches to be used for investigating this specific topic.

These results are found to be robust across a range of CMIP6 models. This in turns provides some confidence for using future hydroclimatic trajectories derived from climate simulations under various emissions scenarios (O'Neill et al. 2016) as a far-from-perfect but nevertheless meaningful basis for building adaptation strategies to rainfall regime changes.

Acknowledgments. The authors thank Frédéric Hourdin for useful discussions and the two anonymous reviewers for their insightful comments. They are also grateful to the late Françoise Guichard for initial discussions that demonstrate once again its will and ability for bridging the gaps between the various communities of scientists involved in climate research. The authors acknowledge the World Climate Research Programme's Working Group on climate modeling for coordination and promotion of CMIP6, and the climate modeling institutions for producing and making available the model outputs. The authors declare no competing interest.

Data availability statement. Model data were acquired on the CICLAD server (http://ciclad-web.ipsl.jussieu.fr/). The daily rain gauge data are the property of the national meteorological agencies and as such are subject to third-party restrictions and are not freely available.

APPENDIX A

Calculation of Standardized Indices

a. Annual total

The standardized index for annual totals (SI ATOT) is computed as follows: the interannual mean of annual totals is computed at each station ($\overline{\text{ATOT}_j}$) and averaged across stations, yielding $\overline{\text{ATOT}_S}$. The regional anomaly time series is computed as follows:

$$\text{ATOT}(i) = \overline{\text{ATOT}_S} + \overset{j}{E}[\text{ATOT}_j(i) - \overline{\text{ATOT}_j}], \tag{A1}$$

where i stands for year and j stands for station/grid point. Standardization is computed with the mean and standard deviation of the ATOT time series over the period 1979–2008. All stations having at least 50 valid years over the period 1950–2014 are used for the SI ATOT computation.

b. Daily rainfall annual maxima

Calculation of standardized index for annual maxima of daily rainfall (SI AMAX) is based on a regional GEV (RGEV) model wherein the location and scale parameters vary linearly with latitude [Eq. (A2)] to account for the well-marked south–north gradient in these two parameters (after Panthou et al. 2012). The model is inferred with a maximum likelihood estimation:

$$\begin{cases} \mu(\text{lat}) = \mu_0 + \mu_1 \times \text{lat} \\ \sigma(\text{lat}) = \sigma_0 + \sigma_1 \times \text{lat}\,. \\ \xi \end{cases} \tag{A2}$$

The RGEV model used for observations includes a linear dependence to longitude for μ and σ:

$$\begin{cases} \mu(\text{lat},\text{lon}) = \mu_0 + \mu_1 \times \text{lat} + \mu_2 \times \text{lon} \\ \sigma(\text{lat},\text{lon}) = \sigma_0 + \sigma_1 \times \text{lat} + \sigma_2 \times \text{lon}\,. \\ \xi \end{cases} \tag{A3}$$

From the RGEV model CDF at station/grid point j, F_j, the frequency of the annual maxima of daily rainfall $z_{i,j}$ is computed, for each year i:

$$p(i,j) = F_j(z_{i,j}). \tag{A4}$$

By construction, the $p(i, j)$ are uniformly distributed. For each year the mean and standard deviation across stations of the p values is computed. The SI AMAX is obtained by standardizing these time series with respect to their mean and standard deviation over the period 1979–2008. All stations having at least 24 years over the 1979–2008 period are used for fitting of the RGEV model.

The return level i_T, with return period T, is the daily rainfall amount that has a $1/T$ chance to occur each year over the period used to fit the model. It can be computed as follows:

$$i_T = \mu + \frac{\sigma}{\xi}\left\{\left[-\log\left(1 - \frac{1}{T}\right)\right]^{-\xi} - 1\right\}. \tag{A5}$$

c. Wet days intensity and occurrence

The methodology used to obtain the regional mean daily rainfall intensity and number of wet days, described in the supplementary material of Panthou et al. (2018), goes as follows (we denote X the variable to compute):

- At each location j (station/grid point) having Y_j years available, the interannual mean is computed:

$$\overline{X_j} = \frac{1}{Y_j}\sum_{i}^{Y_j} X_i. \tag{A6}$$

- The regional mean of the pointwise interannual means is computed: $\overline{X_S} = \overset{j}{E}[\overline{X_j}]$.
- The regional mean time series is obtained as follows:

$$\overline{X(i)} = \overline{X_S} + \overset{j}{E}[X_j(i) - \overline{X_j}]. \tag{A7}$$

The index is then standardized using the mean ($\overline{\overline{X}}$) and standard deviation ($\sigma_{\overline{X}}$) over the reference period:

$$X = \frac{\overline{X} - \overline{\overline{X}}}{\sigma_{\overline{X}}}. \tag{A8}$$

APPENDIX B

Regional Nonstationary GEV (RNSGEV) Model

The RGEV model parameters [Eq. (A2)] are expressed as a linear function of time to account for systematic changes in

rainfall extremes over a given period. The RNSGEV model parameters read as follows:

$$\begin{cases} \mu(\text{lat}, \text{lon}, t) = (\mu_0 + \mu_1 \times \text{lat} + \mu_2 \times \text{lon}) \times (1 + \alpha_3 \times t) \\ \sigma(\text{lat}, \text{lon}, t) = (\sigma_0 + \sigma_1 \times \text{lat} + \sigma_2 \times \text{lon}) \times (1 + \alpha_3 \times t) \\ \xi \end{cases}. \tag{B1}$$

Similarly to Eq. (A5), the space- and time-dependent return level $i_T(\text{lat}, \text{lon}, t)$ with return period T is the daily rainfall amount that has a $1/T$ chance to occur at year t and location (lat, lon). It can be computed as follows:

$$i_T(\text{lat}, \text{lon}, t) = \mu(\text{lat}, \text{lon}, t) + \frac{\sigma(\text{lat}, \text{lon}, t)}{\xi} \times \left\{ \left[-\log\left(1 - \frac{1}{T}\right) \right]^{-\xi} - 1 \right\}, \tag{B2}$$

where $\mu(\text{lat}, \text{lon}, t)$, $\sigma(\text{lat}, \text{lon}, t)$, and ξ are the RNSGEV model parameters.

The model inference uncertainty is estimated with the semiparametric bootstrap resampling technique described in Chagnaud et al. (2021). The 50% confidence intervals of the T-yr return level trends are quantified as the 25th–75th percentile range across 200 sets of bootstrapped trends.

REFERENCES

Ackerley, D., B. B. B. Booth, S. H. E. Knight, E. J. Highwood, D. J. Frame, M. R. Allen, and D. P. Rowell, 2011: Sensitivity of twentieth-century Sahel rainfall to sulfate aerosol and CO_2 forcing. *J. Climate*, **24**, 4999–5014, https://doi.org/10.1175/JCLI-D-11-00019.1.

Allan, R. P., and Coauthors, 2020: Advances in understanding large-scale responses of the water cycle to climate change. *Ann. N. Y. Acad. Sci.*, **1472**, 49–75, https://doi.org/10.1111/nyas.14337.

Allen, M. R., and W. J. Ingram, 2002: Constraints on future changes in climate and the hydrologic cycle. *Nature*, **419**, 224–232, https://doi.org/10.1038/nature01092.

Andrews, T., and Coauthors, 2019: Forcings, feedbacks, and climate sensitivity in HadGEM3-GC3.1 and UKESM1. *J. Adv. Model. Earth Syst.*, **11**, 4377–4394, https://doi.org/10.1029/2019MS001866.

Berthou, S., D. P. Rowell, E. J. Kendon, M. J. Roberts, R. A. Stratton, J. A. Crook, and C. Wilcox, 2019: Improved climatological precipitation characteristics over West Africa at convection-permitting scales. *Climate Dyn.*, **53**, 1991–2011, https://doi.org/10.1007/s00382-019-04759-4.

Biasutti, M., and A. Giannini, 2006: Robust Sahel drying in response to late 20th century forcings. *Geophys. Res. Lett.*, **33**, L11706, https://doi.org/10.1029/2006GL026067.

Bonnet, R., O. Boucher, J. Deshayes, G. Gastineau, F. Hourdin, J. Mignot, J. Servonnat, and D. Swingedouw, 2021: Presentation and evaluation of the IPSL-CM6A-LR ensemble of extended historical simulations. *J. Adv. Model. Earth Syst.*, **13**, e2021MS002565, https://doi.org/10.1029/2021MS002565.

Booth, B. B. B., N. J. Dunstone, P. R. Halloran, T. Andrews, and N. Bellouin, 2012: Aerosols implicated as a prime driver of twentieth-century North Atlantic climate variability. *Nature*, **484**, 228–232, https://doi.org/10.1038/nature10946.

Boucher, O., and Coauthors, 2020: Presentation and evaluation of the IPSL-CM6A-LR climate model. *J. Adv. Model. Earth Syst.*, **12**, e2019MS002010, https://doi.org/10.1029/2019MS002010.

Chagnaud, G., H. Gallée, T. Lebel, G. Panthou, and T. Vischel, 2020: A boundary forcing sensitivity analysis of the West African monsoon simulated by the Modèle Atmosphérique Régional. *Atmosphere*, **11**, 191, https://doi.org/10.3390/atmos11020191.

——, G. Panthou, T. Vischel, J. Blanchet, and T. Lebel, 2021: A unified statistical framework for detecting trends in multi-timescale precipitation extremes: Application to nonstationary intensity-duration-frequency curves. *Theor. Appl. Climatol.*, **145**, 839–860, https://doi.org/10.1007/s00704-021-03650-9.

——, ——, ——, and T. Lebel, 2022: A synthetic view of rainfall intensification in the West African Sahel. *Environ. Res. Lett.*, **17**, 044005, https://doi.org/10.1088/1748-9326/ac4a9c.

Chang, C.-Y., J. C. H. Chiang, M. F. Wehner, A. R. Friedman, and R. Ruedy, 2011: Sulfate aerosol control of tropical Atlantic climate over the twentieth century. *J. Climate*, **24**, 2540–2555, https://doi.org/10.1175/2010JCLI4065.1.

Dai, A., P. J. Lamb, K. E. Trenberth, M. Hulme, P. D. Jones, and P. Xie, 2004: The recent Sahel drought is real. *Int. J. Climatol.*, **24**, 1323–1331, https://doi.org/10.1002/joc.1083.

Danabasoglu, G., 2019: NCAR CESM2 model output prepared for CMIP6 CMIP historical. Earth System Grid Federation, https://doi.org/10.22033/ESGF/CMIP6.7627.

Descroix, L., and Coauthors, 2018: Evolution of surface hydrology in the Sahelo-Sudanian strip: An updated review. *Water*, **10**, 748, https://doi.org/10.3390/w10060748.

Deser, C., A. Phillips, V. Bourdette, and H. Teng, 2012: Uncertainty in climate change projections: The role of internal variability. *Climate Dyn.*, **38**, 527–546, https://doi.org/10.1007/s00382-010-0977-x.

Di Baldassarre, G., A. Montanari, H. Lins, D. Koutsoyiannis, L. Brandimarte, and G. Bloöschl, 2010: Flood fatalities in Africa: From diagnosis to mitigation. *Geophys. Res. Lett.*, **37**, L22402, https://doi.org/10.1029/2010GL045467.

Doblas-Reyes, F. J., and Coauthors, 2021: Linking global to regional climate change. *Climate Change 2021: The Physical Science Basis*, V. Masson-Delmotte et al., Eds., Cambridge University Press, 1363–1512.

Dong, B., and R. Sutton, 2015: Dominant role of greenhouse-gas forcing in the recovery of Sahel rainfall. *Nat. Climate Change*, **5**, 757–760, https://doi.org/10.1038/nclimate2664.

Elagib, N. A., I. S. A. Zayed, S. A. G. Saad, and M. I. Mahmood, M. Basheer, and A. H. Fink, 2021: Debilitating floods in the Sahel are becoming frequent. *J. Hydrol.*, **599**, 126362, https://doi.org/10.1016/j.jhydrol.2021.126362.

Evan, A. T., C. Flamant, C. Lavaysse, C. Kocha, and A. Saci, 2015: Water vapor–forced greenhouse warming over the Sahara Desert and the recent recovery from the Sahelian drought. *J. Climate*, **28**, 108–123, https://www.jstor.org/stable/26194661.

Eyring, V., S. Bony, G. A. Meehl, C. A. Senior, B. Stevens, R. J. Stouffer, and K. E. Taylor, 2016: Overview of the Coupled Model Intercomparison Project phase 6 (CMIP6) experimental design and organization. *Geosci. Model Dev.*, **9**, 1937–1958, https://doi.org/10.5194/gmd-9-1937-2016.

Fitzpatrick, R. G. J., and Coauthors, 2020: What drives the intensification of mesoscale convective systems over the West African Sahel under climate change? *J. Climate*, **33**, 3151–3172, https://doi.org/10.1175/JCLI-D-19-0380.1.

Fläschner, D., T. Mauritsen, and B. Stevens, 2016: Understanding the intermodel spread in global-mean hydrological sensitivity. *J. Climate*, **29**, 801–817, https://doi.org/10.1175/JCLI-D-15-0351.1.

Fontaine, B., P. Roucou, and P.-A. Monerie, 2011: Changes in the African monsoon region at medium-term time horizon using 12 AR4 coupled models under the A1b emissions scenario. *Atmos. Sci. Lett.*, **12**, 83–88, https://doi.org/10.1002/asl.321.

Friedman, A. R., G. C. Hegerl, A. P. Schurer, S.-Y. Lee, W. Kong, W. Cheng, and J. C. H. Chiang, 2020: Forced and unforced decadal behavior of the interhemispheric SST contrast during the instrumental period (1881–2012): Contextualizing the late 1960s–early 1970s shift. *J. Climate*, **33**, 3487–3509, https://doi.org/10.1175/JCLI-D-19-0102.1.

Gaetani, M., C. Flamant, S. Bastin, S. Janicot, C. Lavaysse, F. Hourdin, P. Braconnot, and S. Bony, 2017: West African monsoon dynamics and precipitation: The competition between global SST warming and CO_2 increase in CMIP5 idealized simulations. *Climate Dyn.* **48**, 1353–1373, https://doi.org/10.1007/s00382-016-3146-z.

Giannini, A., 2010: Mechanisms of climate change in the semiarid African Sahel: The local view. *J. Climate*, **23**, 743–756, https://doi.org/10.1175/2009JCLI3123.1.

——, and A. Kaplan, 2019: The role of aerosols and greenhouse gases in Sahel drought and recovery. *Climatic Change*, **152**, 449–466, https://doi.org/10.1007/s10584-018-2341-9.

——, S. Salack, T. Lodoun, A. Ali, A. T. Gaye, and O. Ndiaye, 2013: A unifying view of climate change in the Sahel linking intra-seasonal, interannual and longer time scales. *Environ. Res. Lett.*, **8**, 024010, https://doi.org/10.1088/1748-9326/8/2/024010.

Gillett, N. P., and Coauthors, 2016: The detection and attribution model intercomparison project (DAMIP v1.0) contribution to CMIP6. *Geosci. Model Dev.*, **9**, 3685–3697, https://doi.org/10.5194/gmd-9-3685-2016.

Hagos, S. M., L. R. Leung, O. A. Garuba, C. Demott, B. Harrop, J. Lu, and M.-S. Ahn, 2021: The relationship between precipitation and precipitable water in CMIP6 simulations and implications for tropical climatology and change. *J. Climate*, **34**, 1587–1600, https://doi.org/10.1175/JCLI-D-20-0211.1.

Hawkins, E., and R. Sutton, 2009: The potential to narrow uncertainty in regional climate predictions. *Bull. Amer. Meteor. Soc.*, **90**, 1095–1108, https://doi.org/10.1175/2009BAMS2607.1.

——, and ——, 2011: The potential to narrow uncertainty in projections of regional precipitation change. *Climate Dyn.*, **37**, 407–418, https://doi.org/10.1007/s00382-010-0810-6.

Hegerl, G. C., and Coauthors, 2019: Causes of climate change over the historical record. *Environ. Res. Lett.*, **14**, 123006, https://doi.org/10.1088/1748-9326/ab4557.

Held, I. M., and B. J. Soden, 2006: Robust responses of the hydrological cycle to global warming. *J. Climate*, **19**, 5686–5699, https://doi.org/10.1175/JCLI3990.1.

Hodson, D. L. R., and Coauthors, 2022: Coupled climate response to Atlantic multidecadal variability in a multi-model multi-resolution ensemble. *Climate Dyn.*, **59**, 805–836, https://doi.org/10.1007/s00382-022-06157-9.

Hoerling, M., J. Hurrell, J. Eischeid, and A. Phillips, 2006: Detection and attribution of twentieth-century northern and southern African rainfall change. *J. Climate*, **19**, 3989–4008, https://doi.org/10.1175/JCLI3842.1.

Hoesly, R. M., and Coauthors, 2018: Historical (1750–2014) anthropogenic emissions of reactive gases and aerosols from the community emissions data system (CEDS). *Geosci. Model Dev.*, **11**, 369–408, https://doi.org/10.5194/gmd-11-369-2018.

Hulme, M., 2001: Climatic perspectives on Sahelian desiccation: 1973–1998. *Global Environ. Change*, **11**, 19–29, https://doi.org/10.1016/S0959-3780(00)00042-X.

IPCC, 2021: Summary for policymakers. *Climate Change 2021: The Physical Science Basis*, V. Masson-Delmotte et al., Eds., Cambridge University Press, 3–32, https://doi.org/10.1017/9781009157896.001.

Laurent, H., N. D'Amato, and T. Lebel, 1998: How important is the contribution of the mesoscale convective complexes to the Sahelian rainfall? *Phys. Chem. Earth*, **23**, 629–633, https://doi.org/10.1016/S0079-1946(98)00099-8.

Lavaysse, C., C. Flamant, A. Evan, S. Janicot, and M. Gaetani, 2016: Recent climatological trend of the Saharan heat low and its impact on the West African climate. *Climate Dyn.*, **47**, 3479–3498, https://doi.org/10.1007/s00382-015-2847-z.

Le Barbé, L., T. Lebel, and D. Tapsoba, 2002: Rainfall variability in West Africa during the years 1950–90. *J. Climate*, **15**, 187–202, https://doi.org/10.1175/1520-0442(2002)015<0187:RVIWAD>2.0.CO;2.

Lebel, T., and A. Ali, 2009: Recent trends in the central and western Sahel rainfall regime (1990–2007). *J. Hydrol.*, **375**, 52–64, https://doi.org/10.1016/j.jhydrol.2008.11.030.

Lehner, F., C. Deser, N. Maher, J. Marotzke, E. M. Fischer, L. Brunner, R. Knutti, and E. Hawkins, 2020: Partitioning climate projection uncertainty with multiple large ensembles and CMIP5/6. *Earth Syst. Dyn.* **11**, 491–508, https://doi.org/10.5194/esd-11-491-2020.

Lochbihler, K., G. Lenderink, and A. P. Siebesma, 2019: Response of extreme precipitating cell structures to atmospheric warming. *J. Geophys. Res. Atmos.*, **124**, 6904–6918, https://doi.org/10.1029/2018JD029954.

Lyu, K., and J.-Y. Yu, 2017: Climate impacts of the Atlantic multidecadal oscillation simulated in the CMIP5 models: A reevaluation based on a revised index. *Geophys. Res. Lett.*, **44**, 3867–3876, https://doi.org/10.1002/2017GL072681.

Marvel, K., M. Biasutti, and C. Bonfils, 2020: Fingerprints of external forcings on Sahel rainfall: Aerosols, greenhouse gases, and model-observation discrepancies. *Environ. Res. Lett.*, **15**, 084023, https://doi.org/10.1088/1748-9326/ab858e.

Mauritsen, T., and Coauthors, 2019: Developments in the MPI-M Earth System Model version 1.2 (MPI-ESM1.2) and its response to increasing CO_2. *J. Adv. Model. Earth Syst.*, **11**, 998–1038, https://doi.org/10.1029/2018MS001400.

Menary, M. B., and Coauthors, 2020: Aerosol-forced AMOC changes in CMIP6 historical simulations. *Geophys. Res. Lett.*, **47**, e2020GL088166, https://doi.org/10.1029/2020GL088166.

Mohino, E., S. Janicot, and J. Bader, 2011: Sahel rainfall and decadal to multi-decadal sea surface temperature variability. *Climate Dyn.*, **37**, 419–440, https://doi.org/10.1007/s00382-010-0867-2.

——, N. Keenlyside, and H. Pohlmann, 2016: Decadal prediction of Sahel rainfall: Where does the skill (or lack thereof) come from? *Climate Dyn.*, **47**, 3593–3612, https://doi.org/10.1007/s00382-016-3416-9.

Monerie, P.-A., B. Fontaine, and P. Roucou, 2012: Expected future changes in the African monsoon between 2030 and 2070 using some CMIP3 and CMIP5 models under a medium-low RCP scenario. *J. Geophy. Res. Atmos.*, **117**, D16111, https://doi.org/10.1029/2012JD017510.

——, B. Pohl, and M. Gaetani, 2021: The fast response of Sahel precipitation to climate change allows effective mitigation action. *npj Climate Atmos. Sci.*, **4**, 24, https://doi.org/10.1038/s41612-021-00179-6.

Nicholson, S. E., 2005: On the question of the "recovery" of the rains in the West African Sahel. *J. Arid Environ.*, **63**, 615–641, https://doi.org/10.1016/j.jaridenv.2005.03.004.

——, A. H. Fink, and C. Funk, 2018: Assessing recovery and change in West Africa's rainfall regime from a 161-year record. *Int. J. Climatol.*, **38**, 3770–3786, https://doi.org/10.1002/joc.5530.

O'Neill, B. C., and Coauthors, 2016: The scenario model intercomparison project (ScenarioMIP) for CMIP6. *Geosci. Model Dev.*, **9**, 3461–3482, https://doi.org/10.5194/gmd-9-3461-2016.

Pall, P., M. R. Allen, and D. A. Stone, 2007: Testing the Clausius–Clapeyron constraint on changes in extreme precipitation under CO_2 warming. *Climate Dyn.*, **28**, 351–363, https://doi.org/10.1007/s00382-006-0180-2.

Panthou, G., T. Vischel, T. Lebel, J. Blanchet, G. Quantin, and A. Ali, 2012: Extreme rainfall in West Africa: A regional modeling. *Water Resour. Res.*, **48**, W08501, https://doi.org/10.1029/2012WR012052.

——, ——, and ——, 2014: Recent trends in the regime of extreme rainfall in the Central Sahel. *Int. J. Climatol.*, **34**, 3998–4006, https://doi.org/10.1002/joc.3984.

——, and Coauthors, 2018: Rainfall intensification in tropical semi-arid regions: The Sahelian case. *Environ. Res. Lett.*, **13**, 064013, https://doi.org/10.1088/1748-9326/aac334.

Park, J.-Y., J. Bader, and D. Matei, 2016: Anthropogenic Mediterranean warming essential driver for present and future Sahel rainfall. *Nat. Climate Change*, **6**, 941–945, https://doi.org/10.1038/nclimate3065.

Pendergrass, A. G., 2020: The global-mean precipitation response to CO_2-induced warming in CMIP6 models. *Geophys. Res. Lett.*, **47**, e2020GL089964, https://doi.org/10.1029/2020GL089964.

——, and D. L. Hartmann, 2014: The atmospheric energy constraint on global-mean precipitation change. *J. Climate*, **27**, 757–768, https://doi.org/10.1175/JCLI-D-13-00163.1.

Porkka, M., L. Wang-Erlandsson, G. Destouni, A. M. L. Ekman, J. Rockström, and L. J. Gordon, 2021: Is wetter better? Exploring agriculturally-relevant rainfall characteristics over four decades in the Sahel. *Environ. Res. Lett.*, **16**, 035002, https://doi.org/10.1088/1748-9326/abdd57.

Pörtner, H.-O., and Coauthors, 2022: *Climate Change 2022: Impacts, Adaptation, and Vulnerability.* Cambridge University Press, 3056 pp., https://doi.org/10.1017/9781009325844.

Prein, A. F., C. Liu, K. Ikeda, S. B. Trier, R. M. Rasmussen, G. J. Holland, and M. P. Clark, 2017: Increased rainfall volume from future convective storms in the U.S. *Nat. Climate Change*, **7**, 880–884, https://doi.org/10.1038/s41558-017-0007-7.

Räisänen, J., 2001: CO_2-induced climate change in CMIP2 experiments: Quantification of agreement and role of internal variability. *J. Climate*, **14**, 2088–2104, https://doi.org/10.1175/1520-0442(2001)014<2088:CICCIC>2.0.CO;2.

Richter, I., and S.-P. Xie, 2008: On the origin of equatorial Atlantic biases in coupled general circulation models. *Climate Dyn.*, **31**, 587–598, https://doi.org/10.1007/s00382-008-0364-z.

——, and H. Tokinaga, 2020: An overview of the performance of CMIP6 models in the tropical Atlantic: Mean state, variability, and remote impacts. *Climate Dyn.*, **55**, 2579–2601, https://doi.org/10.1007/s00382-020-05409-w.

——, S.-P. Xie, S. K. Behera, T. Doi, and Y. Masumoto, 2014: Equatorial Atlantic variability and its relation to mean state biases in CMIP5. *Climate Dyn.*, **42**, 171–188, https://doi.org/10.1007/s00382-012-1624-5.

Rodríguez-Fonseca, B., and Coauthors, 2015: Variability and predictability of West African droughts: A review on the role of sea surface temperature anomalies. *J. Climate*, **28**, 4034–4060, https://doi.org/10.1175/JCLI-D-14-00130.1.

Rotstayn, L. D., and U. Lohmann, 2002: Tropical rainfall trends and the indirect aerosol effect. *J. Climate*, **15**, 2103–2116, https://doi.org/10.1175/1520-0442(2002)015<2103:TRTATI>2.0.CO;2.

Salack, S., A. Giannini, M. Diakhaté, A. T. Gaye, and B. Muller, 2014: Oceanic influence on the sub-seasonal to interannual timing and frequency of extreme dry spells over the West African Sahel. *Climate Dyn.*, **42**, 189–201, https://doi.org/10.1007/s00382-013-1673-4.

——, C. Klein, A. Giannini, B. Sarr, O. N. Worou, N. Belko, J. Bliefernicht, and H. Kunstman, 2016: Global warming induced hybrid rainy seasons in the Sahel. *Environ. Res. Lett.*, **11**, 104008, https://doi.org/10.1088/1748-9326/11/10/104008.

Sanogo, S., A. H. Fink, J. A. Omotosho, A. Ba, R. Redl, and V. Ermert, 2015: Spatio-temporal characteristics of the recent rainfall recovery in West Africa. *Int. J. Climatol.*, **35**, 4589–4605, https://doi.org/10.1002/joc.4309.

Seland, O., and Coauthors, 2019: NCC NorESM2-LM model output prepared for CMIP6 CMIP historical. Earth System Grid Federation, https://doi.org/10.22033/ESGF/CMIP6.8036.

Sellar, A. A., and Coauthors, 2019: UKESM1: Description and evaluation of the U.K. Earth system model. *J. Adv. Model. Earth Syst.*, **11**, 4513–4558, https://doi.org/10.1029/2019MS001739.

Shin, S.-I., and P. D. Sardeshmukh, 2011: Critical influence of the pattern of Tropical Ocean warming on remote climate trends. *Climate Dyn.*, **36**, 1577–1591, https://doi.org/10.1007/s00382-009-0732-3.

Stephens, G. L., and T. D. Ellis, 2008: Controls of global-mean precipitation increases in global warming GCM experiments. *J. Climate*, **21**, 6141–6155, https://doi.org/10.1175/2008JCLI2144.1.

Tatebe, H., and Coauthors, 2019: Description and basic evaluation of simulated mean state, internal variability, and climate sensitivity in MIROC6. *Geosci. Model Dev.*, **12**, 2727–2765, https://doi.org/10.5194/gmd-12-2727-2019.

Taylor, C. M., and Coauthors, 2017: Frequency of extreme Sahelian storms tripled since 1982 in satellite observations. *Nature*, **544**, 475–478, https://doi.org/10.1038/nature22069.

Ting, M., Y. Kushnir, R. Seager, and C. Li, 2009: Forced and internal twentieth-century SST trends in the North Atlantic. *J. Climate*, **22**, 1469–1481, https://doi.org/10.1175/2008JCLI2561.1.

——, ——, ——, and ——, 2011: Robust features of Atlantic multi-decadal variability and its climate impacts. *Geophys. Res. Lett.*, **38**, L17705, https://doi.org/10.1029/2011GL048712.

Tramblay, Y., G. Villarini, and W. Zhang, 2020: Observed changes in flood hazard in Africa. *Environ. Res. Lett.*, **15**, 1040b5, https://doi.org/10.1088/1748-9326/abb90b.

Trenberth, K. E., 1999: Conceptual framework for changes of extremes of the hydrological cycle with climate change. *Climatic Change*, **42**, 327–339, https://doi.org/10.1023/A:1005488920935.

——, 2011: Changes in precipitation with climate change. *Climate Res.*, **47**, 123–138, https://doi.org/10.3354/cr00953.

——, A. Dai, R. M. Rasmussen, and D. B. Parsons, 2003: The changing character of precipitation. *Bull. Amer. Meteor. Soc.*, **84**, 1205–1218, https://doi.org/10.1175/BAMS-84-9-1205.

Voldoire, A., and Coauthors, 2019: Evaluation of CMIP6 DECK experiments with CNRM-CM6-1. *J. Adv. Model. Earth Syst.*, **11**, 2177–2213, https://doi.org/10.1029/2019MS001683.

Volodin, E. M., and Coauthors, 2017: Simulation of modern climate with the new version of the INM RAS climate model.

Izv., Atmos. Oceanic Phys., **53**, 142–155, https://doi.org/10.1134/S0001433817020128.

Wilcox, C., and Coauthors, 2018: Trends in hydrological extremes in the Senegal and Niger Rivers. *J. Hydrol.*, **566**, 531–545, https://doi.org/10.1016/j.jhydrol.2018.07.063.

Wills, R. C. J., K. C. Armour, D. S. Battisti, and D. L. Hartmann, 2019: Ocean–atmosphere dynamical coupling fundamental to the Atlantic multidecadal oscillation. *J. Climate*, **32**, 251–272, https://doi.org/10.1175/JCLI-D-18-0269.1.

Yan, X., R. Zhang, and T. R. Knutson, 2018: Underestimated AMOC variability and implications for AMV and predictability in CMIP models. *Geophys. Res. Lett.*, **45**, 4319–4328, https://doi.org/10.1029/2018GL077378.

Yukimoto, S., and Coauthors, 2019: The Meteorological Research Institute Earth System Model version 2.0, MRI-ESM2.0: Description and basic evaluation of the physical component. *J. Meteor. Soc. Japan*, **97**, 931–965, https://dsoi.org/10.2151/jmsj.2019-051.

Zhang, R., and T. L. Delworth, 2006: Impact of Atlantic multidecadal oscillations on India/Sahel rainfall and Atlantic hurricanes. *Geophys. Res. Lett.*, **33**, L17712, https://doi.org/10.1029/2006GL026267.

Zhou, T., J. Lu, W. Zhang, and Z. Chen, 2020: The sources of uncertainty in the projection of global land monsoon precipitation. *Geophys. Res. Lett.*, **47**, e2020GL088415, https://doi.org/10.1029/2020GL088415.

Ziehn, T., and Coauthors, 2020: The Australian Earth system model: ACCESS-ESM1.5. *J. South. Hemisphere Earth Syst. Sci.*, **70**, 193–214, https://doi.org/10.1071/ES19035.